

Liquid flow and control without solid walls

<https://doi.org/10.1038/s41586-020-2254-4>

Received: 1 July 2018

Accepted: 26 February 2020

Published online: 6 May 2020

 Check for updates

Peter Dunne^{1,2,8}, Takuji Adachi^{1,3,8}, Arvind Arun Dev², Alessandro Sorrenti^{1,4}, Lucas Giacchetti¹, Anne Bonnin⁵, Catherine Bourdon⁶, Pierre H. Mangin⁶, J. M. D. Coey⁷, Bernard Doudin² & Thomas M. Hermans^{1✉}

When miniaturizing fluidic circuitry, the solid walls of the fluid channels become increasingly important¹ because they limit the flow rates achievable for a given pressure drop, and they are prone to fouling². Approaches for reducing the wall interactions include hydrophobic coatings³, liquid-infused porous surfaces^{4–6}, nanoparticle surfactant jamming⁷, changes to surface electronic structure⁸, electrowetting^{9,10}, surface tension pinning^{11,12} and use of atomically flat channels¹³. A better solution may be to avoid the solid walls altogether. Droplet microfluidics and sheath flow achieve this but require continuous flow of the central liquid and the surrounding liquid^{1,14}. Here we demonstrate an approach in which aqueous liquid channels are surrounded by an immiscible magnetic liquid, both of which are stabilized by a quadrupolar magnetic field. This creates self-healing, non-clogging, anti-fouling and near-frictionless liquid-in-liquid fluidic channels. Manipulation of the field provides flow control, such as valving, splitting, merging and pumping. The latter is achieved by moving permanent magnets that have no physical contact with the liquid channel. We show that this magnetostatic pumping method can be used to transport whole human blood with very little damage due to shear forces. Haemolysis (rupture of blood cells) is reduced by an order of magnitude compared with traditional peristaltic pumping, in which blood is mechanically squeezed through a plastic tube. Our liquid-in-liquid approach provides new ways to transport delicate liquids, particularly when scaling channels down to the micrometre scale, with no need for high pressures, and could also be used for microfluidic circuitry.

To avoid contact with the walls of a device, magnetic forces can be used to levitate particles or live cells in a paramagnetic liquid¹⁵. Nearly wall-less microfluidic channels have been demonstrated in which continuous ‘magnetic antitubes’ of water surrounded by an aqueous paramagnetic salt solution were stabilized¹⁶ by using an electromagnet and iron tracks. However, the antitube lifetime was limited by ion interdiffusion between the two liquids, the salts were toxic, and contact with one stationary wall containing the track could not be avoided. Here we overcome these limitations, creating entirely wall-less microfluidic channels consisting of diamagnetic antitubes completely enclosed by immiscible, and in select cases, non-toxic, paramagnetic fluids.

The key to wall-less magnetic confinement is an extended quadrupolar flux source, leading to a null magnetic field along a line at the centre (Fig. 1a, b). Appropriately magnetized Nd₂Fe₁₄B bars are used to define tubular channels, or else custom-made magnet bilayers are waterjet-cut to define more complex fluidic circuitry. The magnetic bars are housed in 3D-printed supports with conventional microfluidic inlet and outlet ports (Fig. 1 and Extended Data Fig. 1). The various magnetic fluids used are listed in Table 1; stronger confinement is achieved with ferrofluids, but optical transparency is possible with our paramagnetic oil, which we call ‘Magoil’. Ferrofluids are colloidal liquids of magnetite (Fe₃O₄) nanoparticles suspended in a carrier fluid, whereas Magoil is a rare-earth-based oil,

inspired by the contrast agents based on diethylenetriaminepentaacetate (DTPA) that are used for magnetic resonance imaging¹⁷ (Extended Data Fig. 2, and Methods). We used commercial ferrofluids (Ferrotec APG311 and EMG900, 2 vol% and 13 vol% magnetite in hydrocarbon oils respectively; and Qfluidics MKC and MD4, 29 vol% magnetite in hydrocarbons and 5 vol% magnetite in perfluorodecalin, respectively).

Aqueous antitubes were typically formed by injecting ferrofluid into water-filled quadrupole channels and were visualized by X-ray imaging and tomography (Fig. 1c, d, f, Extended Data Fig. 3c–e). Tomography images unambiguously reveal the wall-less features, confirmed by visual inspection of transmitted light through antitubes up to 1 m long (Extended Data Fig. 1g). Optical imaging was found to be possible through ferrofluid no more than 200 μm thick and with a high-contrast camera (Extended Data Fig. 3f, g), where we can take advantage of the optical resolution to image the smallest antitube features. We were able to image antitubes in transparent Magoil with standard optical or fluorescent microscopy by adding contrast ink or fluorescent dye to the water antitube, allowing real-time visualization of antitube extrusion and retraction (Supplementary Video 1). Furthermore, the trapped gas bubbles that are often problematic in conventional devices can easily be removed, as their buoyancy in Magoil overcomes the magnetic confinement. For most practical applications, however, ferrofluids are preferred because of their much

¹Université de Strasbourg, CNRS, ISIS, Strasbourg, France. ²Université de Strasbourg, CNRS, IPCMS UMR 7504, Strasbourg, France. ³Department of Physical Chemistry, University of Geneva, Geneva, Switzerland. ⁴Institute for Chemical and Bioengineering, Department of Chemistry and Applied Biosciences, ETH Zürich, Zurich, Switzerland. ⁵Paul Scherrer Institut, Villigen, Switzerland. ⁶Université de Strasbourg, INSERM, EFS Grand-Est, BPPS UMR-S1255, FMST, Strasbourg, France. ⁷School of Physics and CRANN, Trinity College, Dublin, Ireland. ⁸These authors contributed equally: Peter Dunne, Takuji Adachi. ✉e-mail: hermans@unistra.fr

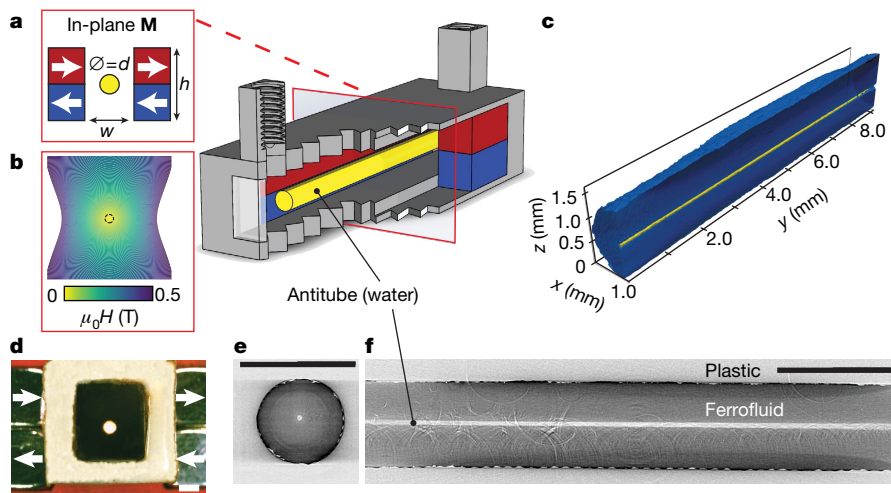


Fig. 1 | Wall-less magnetic confinement in a fluidic channel. **a**, Permanent magnets (red, blue) in an in-plane quadrupolar configuration create a low-field zone at the centre, where an antitube of water (yellow) is stabilized inside an immiscible magnetic liquid (white). **b**, Contour plot of the magnetic field. **c**, Synchrotron X-ray tomographic reconstruction of a water antitube (yellow)

with diameter 81 μm , surrounded by ferrofluid (blue). **d**, Optical end view of a water antitube in ferrofluid. **e**, X-ray end-view cross-section from tomographic data at $y = 4$ mm. **f**, X-ray side-view cross-section from tomographic data at $x = 1$ mm. Scale bars (black/white), 2 mm.

larger magnetic susceptibility χ (Table 1); they can withstand considerable flow rates while remaining confined in the quadrupole (Extended Data Fig. 4a, b). A 1-mm-diameter liquid tube can deliver a flow of about 40 ml min^{-1} . In addition, the phase transfer of magnetite nanoparticles into water is very low, with measured iron concentrations mostly below 1 ppm (see Methods section ‘Quantitative analysis’).

The liquid-in-liquid design offers advantages of stability and robustness for fluid transport. Figure 2a illustrates self-healing after an antitube in ferrofluid was severed with a spatula. Recovery without applied external pressure is rapid (self-healing in Magoil is illustrated in Supplementary Video 2). The antitubes cannot clog: when glass beads are introduced (Fig. 2b), they are easily flushed out. Even a bead much larger than the antitube diameter can be pushed through using minimal pressure (20 mbar; Fig. 2c). The liquid walls of the antitube stretch to avoid clogging and return to their original size when the obstruction is expelled. A change of external pressure alters the antitube diameter. In Extended Data Fig. 4c, d, it can be seen that antitubes remain unchanged with externally applied pressure for an open outlet at atmospheric pressure, but dilate when the same pressure is applied with the outlet closed off. This can also be seen in Fig. 2c, where the tube dilates behind the bead to accommodate the increased local pressure. As a demonstration of anti-fouling behaviour, we used laser light to covalently crosslink a polymer inside an antitube, and were able to remove the resulting solid polymer rod from the outlet of the device (Extended Data Fig. 6a–c, and Supplementary Video 3).

A further advantage of liquid-in-liquid flow is near-frictionless transport with negligible pressure drop. An illustration is shown in Fig. 2d and Supplementary Video 4, where flow of a magnetically confined antitube made of honey (dynamic viscosity $\eta_h = 10 \text{ Pa s}$) is compared with honey flow in a standard tube. We observed an antitube flow of $39.4 \pm 0.7 \text{ g h}^{-1}$, about 70 times faster than the flow through a conventional plastic tube of the same diameter $d = 1.1 \text{ mm}$ ($0.55 \pm 0.10 \text{ g h}^{-1}$). The friction inside a normal tube is quantified by its slip length, defined as the extrapolated distance relative to the boundary where the velocity reduces to zero. Here, the ferrofluid acts as a lubricating layer, with an effective slip length b at the honey/ferrofluid boundary that can be approximated by

$$b = \frac{1}{2} \left[\sqrt{\frac{d^2}{2} (Q_{\text{ND}} + 1)} - d \right] \quad (1)$$

where d is the antitube diameter and Q_{ND} is the non-dimensional flow rate given by

$$Q_{\text{ND}} = \frac{128Q\eta_h}{\pi d^4 \partial P / \partial z} \quad (2)$$

where Q is the flow rate and $\partial P / \partial z$ is the pressure gradient in the flow direction (for derivation, see Methods section ‘Derivation of equations’). Experimentally, we obtain an effective slip length of 4.3 mm, meaning that under these conditions the flow is essentially plug-like. Under the assumption of an infinite channel, the plug-like velocity profile can be calculated, as shown analytically in Extended Data Fig. 4e and using numerical methods in Extended Data Fig. 5a–d, leading to a very long theoretical effective slip length of 8.1 mm. Remarkably, the flow rate of honey through the antitube was 1.5 times as fast as when it fell freely and unconfined (Fig. 2d, centre), probably owing to competition between orifice wetting¹⁸ and the higher hydrostatic pressure due to the greater height of the honey column in the antitube design.

The stable confinement of an antitube, at equilibrium, results from the competing magnetic energy of the confining fluid and the surface energy σ of the magnetic/non-magnetic interface. Inserting these energy densities into the magnetically augmented version of Bernoulli’s equation¹⁹ gives the equilibrium diameter of the antitube (see Methods section ‘Derivation of equilibrium diameter equation’):

$$d = \frac{4\sigma}{2\mu_0 \bar{M} H_1 + \mu_0 M_1^2} \quad (3)$$

where H_1 , M_1 are the magnetic field and magnetization values at the interface, μ_0 is the permeability of free space, and \bar{M} is the field-averaged magnetization of the confining fluid. This equation is valid when the magnetic pressure, $\frac{1}{2}\mu_0 H^2$ is significantly larger than any difference in hydrostatic pressure. It can then be linearized when $M = \chi H$, under the geometrical conditions $w \leq \frac{1}{2}h$ (Fig. 1a) and $d \leq \frac{1}{2}w$, typical of our devices, where w is the spacing between the magnets. The linear model gives the minimum equilibrium dimensionless diameter $d^* = d/w$ as:

$$d^* = \left[\frac{\pi^2}{N_D \chi (\chi + 1)} \right]^{1/3} \quad (4)$$

Table 1 | Characteristics of the magnetic fluids

Magnetic liquid	Susceptibility, χ	Viscosity, η (mPa s)*	Appearance
Magoil	4.7×10^{-4}	600	Transparent
APG311 ferrofluid	0.151	70	Opaque/black
EMG900 ferrofluid	1.67	60	Opaque/black
MKC ferrofluid	1.88	380	Opaque/black
MD4 ferrofluid	0.315	180	Opaque/black

*At a shear rate of 100 s^{-1}

where $N_D = \mu_0 M_r^2 w / \sigma$ is the magnetic confinement number expressing the ratio of magnetic to surface energies (see Methods section ‘Derivation of linear and saturation models’), and M_r is the remanent magnetization of the permanent magnets. Note that a 1,000-fold increase in χ reduces d^* by a factor of 100, revealing the importance of the magnetic susceptibility of the confining fluid.

We have studied how the attainable antitube diameters vary with w for the paramagnetic confinement liquids given in Table 1. There is good agreement between the experimental points for water antitubes and the predictions of equations (3) and (4), using measured susceptibility χ and interface energy σ (Extended Data Table 1). The addition of a surfactant to the water phase, to the magnetic fluid phase or to both²⁰ leads to smaller antitubes since σ is lowered; 1 vol% or 23 mM Span-80, in the ferrofluid, and 1 vol% or 0.58 mM Tween-20 in the aqueous antitube. Although the critical micelle concentrations of Span-80 and Tween-20 in water–hydrocarbon interfaces are 1.2 mM and 0.58 mM, respectively²¹, we did not observe surfactant-induced structure formation. The close agreement is shown in the plot of dimensionless diameters d^* in Fig. 2e where plots of the experimental values versus predicted diameters collapse onto one curve for all ferrofluids, surface tensions and magnet gaps used. The smallest antitube that could be detected so far has $d = 14 \pm 2 \mu\text{m}$, obtained when using a strong ferrofluid, EMG900 (Extended Data Fig. 3g). Our model predicts that antitubes below 1 μm can be stabilized, with a 100- μm magnet spacing and a strong ferrofluid (MKC), but they are currently below the detection limit of our imaging methods.

Magnetic confinement can be used to implement basic microfluidic operations. To make branched antitube devices, we resort to out-of-plane quadrupolar fields, made by waterjet-cutting two stacked $\text{Nd}_2\text{Fe}_{14}\text{B}$ plates (Fig. 3a). The null-field line follows the channel centre independently of the channel angle with respect to the magnets, which is not the case for in-plane quadrupoles (not shown). Symmetric splitting of the flow was demonstrated in a ferrofluid antitube Y-junction (Supplementary Video 7). Merging of the flow at a Y-junction was visualized for antitubes stabilized by Magoil. Remarkably, merging and rapid mixing occurs immediately after a Y-junction (Fig. 3b), similar to mixing in magnetically stabilized aqueous paramagnetic tubes surrounded by water¹⁶. This behaviour is in contrast to the laminar flow observed in a 3D-printed microfluidic chip with the same channel size and geometry as the antitube (Fig. 3c).

As our microfluidic circuits are magnetically defined, we can exploit the fact that structured magnetic fields can be modulated by mechanical or electrical means to impose unique and versatile control of fluidic devices. Valves can be constructed by moving one or two longitudinally magnetized bars towards the quadrupole axis. The valving magnets pinch off the antitube by removing the null field at the centre (Fig. 3d, e), thereby imposing a local magnetic pressure, $P = \mu_0 \mathbf{M} \cdot \mathbf{H}$, and interrupting the liquid flow (see Supplementary Videos 8–10, which plot the calculated 150-mT isovolume surfaces). The burst pressure of these valves was tested with an Elvexys OB1 pressure-driven pump. A single transverse valving magnet could sustain a pressure of 125 mbar, whereas a dual valve (Fig. 3f) withstood 300 mbar. Pumping is an extension of the valving principle; pinch points of magnetic pressure seal off pockets of pumped liquid (for example, water) which are then

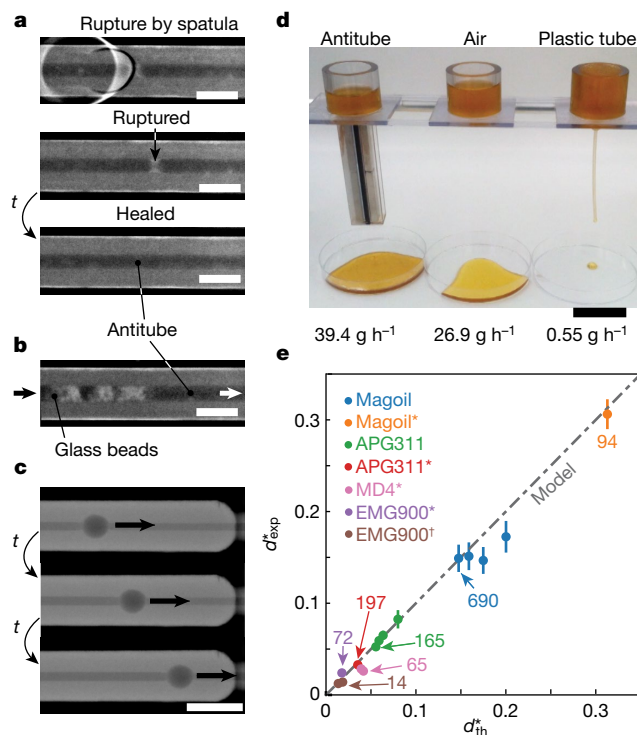


Fig. 2 | Properties and scaling of water antitubes. **a**, Top-view X-ray images illustrating the mechanical rupture of a static tube by a spatula, followed by self-healing. The tube returns to equilibrium, without being under flow, within minutes. **b**, Glass beads (0.6 mm) inserted into a 1.5-mm antitube can be expelled with a slight increase in applied pressure of 20 mbar. **c**, A 2-mm-diameter bead, larger than the antitube diameter ($d = 0.5 \text{ mm}$), does not cause clogging. There is only a small decrease in flow rate (from $30 \mu\text{l min}^{-1}$ to $23 \mu\text{l min}^{-1}$) when the bead is present. **In a–c**, the scale bars are 5 mm. **d**, Comparative flow of honey under gravity (see Supplementary Video 4) through an antitube (left), a normal tube of the same diameter (right) and in free fall (centre; tube open across full diameter). Scale bar, 4 cm. **e**, Plot of experimental dimensionless antitube diameters $d^* = d/w$ (where w is the spacing between the magnets) versus theoretical values calculated from equation (4), for a series of magnetic fluids. Numbers indicate the smallest tube diameters in micrometres. *Water containing 1 vol% Tween-20. †1 vol% Span-80 in the ferrofluid in addition to 1 vol% Tween-20 in the water. For ferrofluid data, each data point represents the average of at least two experiments, for which at least five images were recorded each. For Magoil*, at least 10 snapshots were taken from an experimental video. Error bars are standard deviations.

displaced by the mechanical actuation of the valving magnets. This can be done by sequential excitation of electro- or electro-permanent magnets, or a rotating array of magnetic spokes (see Extended Data Fig. 6d–f). A more sophisticated pump based on radially magnetized arc-segments fixed onto a rotor and stator, and a 3D-printed fluidic support, is illustrated in Fig. 3g, with magnetic field contours shown in Extended Data Fig. 6j. This ‘Qpump’, using MKC ferrofluid, produces pressures of up to 900 mbar and flow rates of $32.7 \pm 0.3 \text{ ml min}^{-1}$ (Supplementary Video 12, Fig. 3h).

Because the antitube inside the Qpump has no solid walls, we expected that magnetostaltic pumping would be gentler than peristaltic pumping, in which a plastic tube is mechanically squeezed by a roller. It is known that blood pumping results in haemolysis: that is, shear-induced rupture of red blood cells that releases haemoglobin^{22–26}. High concentrations of free haemoglobin are cytotoxic and have been associated with clinical complications including an increased incidence of thrombosis, morbidity and mortality^{22–26}. We therefore compared the effects of pumping 6-ml samples of human donor blood (collected on hirudin anticoagulant) at 1.5 ml min^{-1} for 1 h in a closed

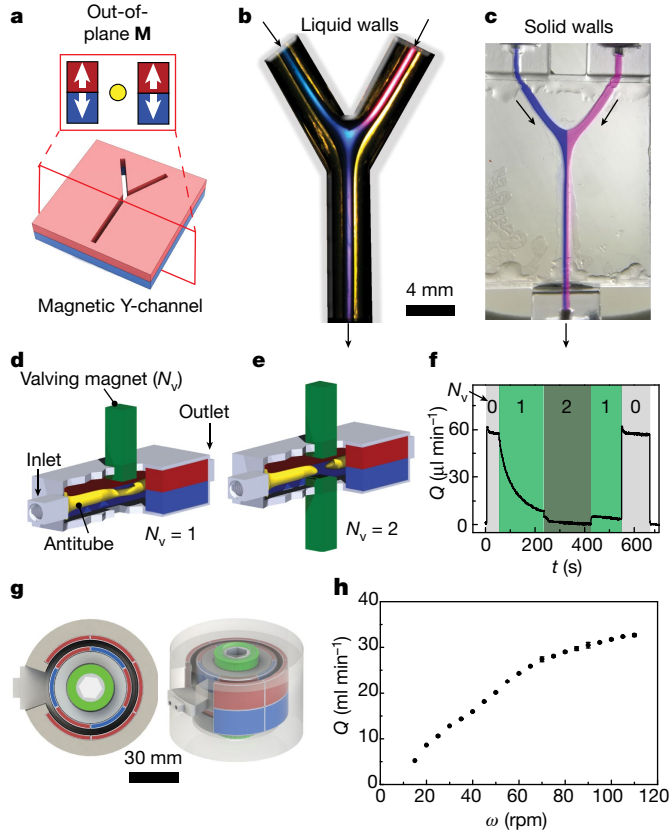


Fig. 3 | Magnetically implemented mixing, valving and pumping.

a, Out-of-plane magnetization configuration for a Y-junction cut in a double magnet sheet. **b**, Optical image of an aqueous antitube stabilized by Tb^{3+} -Magoil. Blue and pink dyes are introduced at the inlets ($300 \mu\text{l min}^{-1}$) and mix immediately upon contact before flowing to the outlet. **c**, Comparison with a normal microfluidic channel, in which no mixing is observed. **d**, **e**, Valving with one magnet ($N_v = 1$, Supplementary Video 9; **d**) or two magnets ($N_v = 2$, Supplementary Video 10; **e**). **f**, Measured flow rate Q under an applied pressure of 100 mbar at the exit port controlled by one or two valving magnets. **g**, Top view and isometric view of a magnetostaltic Qpump with rotating magnetic segments. The orientation of magnetization for the arc segments is radially outward (red) or inward (blue). **h**, Flow rate of water versus rotation rate, ω , of the inner rotor. Error bars represent the standard deviations over three samples.

loop, using either the Qpump or a peristaltic pump (Fig. 4a). Whereas for water sub-ppm transfer of magnetite nanoparticles was observed, for blood $285 \pm 161 \text{ ppm}$ ($\mu\text{g Fe}_3\text{O}_4$ per g blood) was detected (see Methods sections ‘Quantitative analysis of water contamination’ and ‘Blood pumping and analysis’). However, this did not affect haematological parameters such as haematocrit and cell counts of the pumped blood, which were unchanged compared with the peristaltic pump (Fig. 4b and Extended Data Table 2). Moreover, functions of platelets that circulated through the Qpump were unchanged, as they responded normally to agonists such as thrombin-receptor-activating peptides (TRAP) in the widely used light transmission aggregation test (Fig. 4b). Further inspection of platelet morphology by scanning electron microscopy (SEM) confirmed that platelets were intact and normal after pumping (Extended Data Fig. 7a–c). In short, these experiments revealed no adverse effects on whole blood pumped using the Qpump, as compared with a peristaltic pump.

In contrast, a large difference was found in the degree of haemolysis (Fig. 4d, e, Extended Data Fig. 7d). Platelet-rich plasma (PRP) obtained by centrifugation of whole blood is transparent after pumping using the Qpump, but it is bright red after peristaltic pumping (insets,

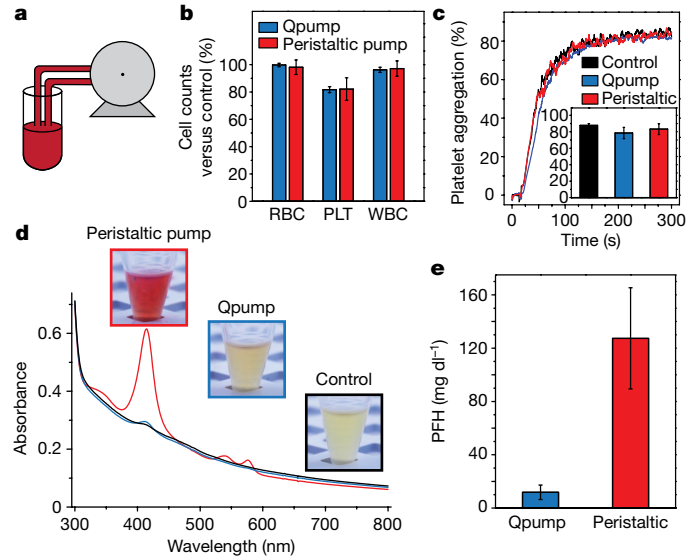


Fig. 4 | Blood pumping by a magnetostaltic pump. Blood was circulated in a closed-loop circuit either by the Qpump (filled with $7\times$ diluted MKC ferrofluid) or a normal peristaltic pump. **a**, Closed-cycle pumping scheme used. **b**, Blood-cell counts (RBC, red blood cells; PLT, platelets; WBC, white blood cells) after pumping normalized versus control blood. **c**, The degree of platelet aggregation activated by TRAP tested for PRP from blood after peristaltic pumping and Qpumping, compared with control blood. Light transmission is minimal before aggregation as platelets scatter light, but upon addition of TRAP the platelets aggregate and transmission increases. **d**, Absorption spectrum of PRP from blood after peristaltic pumping and Qpumping, compared with control blood, 25 times diluted with phosphate buffer. **e**, Plasma-free haemoglobin (PFH) concentration estimated from the absorbance of PRP for Qpump and peristaltic pump. Blood was used from three different anonymous donors (see Methods section ‘Blood pumping and analysis’), and bars show data from at least six measurements. Error bars show standard deviations.

Fig. 4d). From the ultraviolet–visible (UV–vis) absorbance of haemoglobin²⁷ (Fig. 4d), the concentration of plasma-free haemoglobin (PFH) was determined to be $130 \pm 40 \text{ mg dl}^{-1}$ for the peristaltic pump and $12 \pm 5 \text{ mg dl}^{-1}$ for the Qpump (Fig. 4e). The degree of haemolysis is 11 ± 6 times lower for blood pumped by the Qpump than for the traditional peristaltic pump. PFH values greater than 20 mg dl^{-1} are indicative of high haemolysis²⁸, and previous reports on transfusion of packed red blood cells by means of infusion pumps showed PFH values 2–3 orders of magnitude higher²⁶. This indicates that magnetic pumping is a promising way to achieve gentle transportation of blood, or possibly other fragile entities such as antibodies or stem cells. Further studies are planned with a mouse model of extracorporeal membrane oxygenation, using a Qpump instead of a peristaltic pump, to investigate survival rates and possible systemic responses upon ferrofluid contact.

Magnetic control of liquid-in-liquid flow opens new possibilities for microfluidics, allowing new channel shapes and low-pressure cargo transport surpassing the current capabilities of standard methods. We have identified the basic physical quantities controlling the size of confined diamagnetic fluid circuitry and have given examples of key microfluidic device elements. The method promises low-shear flow and pumping, which is of growing importance in biotechnology where delicate cells, proteins and antibodies are commonly damaged by traditional pumps^{29–33}. If scaled up to $5\text{--}7 \text{ l min}^{-1}$ and combined with a gradient–field separator³⁴ to remove traces of transferred magnetite nanoparticles, magnetic blood pumping might be implemented in heart–lung machines during cardiopulmonary bypass surgery, or in devices for extracorporeal membrane oxygenation^{22–25}. At a more fundamental level, we envisage miniaturized fluidic circuits without

solid walls that will be scalable down to the submicrometre level. We can then take advantage of the versatility of magnetic control at the nanoscale to open the door to practical low-pressure nanofluidics^{35–37}.

Online content

Any methods, additional references, Nature Research reporting summaries, source data, extended data, supplementary information, acknowledgements, peer review information; details of author contributions and competing interests; and statements of data and code availability are available at <https://doi.org/10.1038/s41586-020-2254-4>.

1. Tabeling, P. *Introduction to Microfluidics* (Oxford, 2005).
2. Mukhopadhyay, R. When microfluidic devices go bad. *Anal. Chem.* **77**, 429A–432A (2005).
3. Zhao, B., Moore, J. S. & Beebe, D. J. Surface-directed liquid flow inside microchannels. *Science* **291**, 1023–1026 (2001).
4. Wong, T.-S. et al. Bioinspired self-repairing slippery surfaces with pressure-stable omniphobicity. *Nature* **477**, 443–447 (2011).
5. Wang, W. et al. Multifunctional ferrofluid-infused surfaces with reconfigurable multiscale topography. *Nature* **559**, 77–82 (2018).
6. Leslie, D. C. et al. A bioinspired omniphobic surface coating on medical devices prevents thrombosis and biofouling. *Nat. Biotechnol.* **32**, 1134–1140 (2014).
7. Forth, J. et al. Reconfigurable printed liquids. *Adv. Mater.* **30**, 1707603 (2018).
8. Secchi, E. et al. Massive radius-dependent flow slippage in carbon nanotubes. *Nature* **537**, 210–213 (2016).
9. Banerjee, A., Kreit, E., Liu, Y., Heikenfeld, J. & Papautsky, I. Reconfigurable virtual electro-wetting channels. *Lab Chip* **12**, 758 (2012).
10. Choi, K., Ng, A. H. C., Fobel, R. & Wheeler, A. R. Digital microfluidics. *Annu. Rev. Anal. Chem.* **5**, 413–440 (2012).
11. Lee, W. C., Heo, Y. J. & Takeuchi, S. Wall-less liquid pathways formed with three-dimensional microring arrays. *Appl. Phys. Lett.* **101**, 114108 (2012).
12. Walsh, E. J. et al. Microfluidics with fluid walls. *Nat. Commun.* **8**, 816 (2017).
13. Keerthi, A. et al. Ballistic molecular transport through two-dimensional channels. *Nature* **558**, 420–424 (2018).
14. Shang, L., Cheng, Y. & Zhao, Y. Emerging droplet microfluidics. *Chem. Rev.* **117**, 7964–8040 (2017).
15. Zhao, W., Cheng, R., Miller, J. R. & Mao, L. Label-free microfluidic manipulation of particles and cells in magnetic liquids. *Adv. Funct. Mater.* **26**, 3916–3932 (2016).
16. Coey, J. M. D., Aogaki, R., Byrne, F. & Stamenov, P. Magnetic stabilization and vorticity in submillimeter paramagnetic liquid tubes. *Proc. Natl Acad. Sci. USA* **106**, 8811–8817 (2009).
17. Caravan, P., Ellison, J. J., McMurry, T. J. & Lauffer, R. B. Gadolinium(III) chelates as MRI contrast agents: structure, dynamics, and applications. *Chem. Rev.* **99**, 2293–2352 (1999).
18. Ferrand, J., Favreau, L., Joubaud, S. & Freyssingas, E. Wetting effect on Torricelli's law. *Phys. Rev. Lett.* **117**, 248002 (2016).
19. Rosensweig, R. E. *Ferrohydrodynamics* (Dover, 2014).
20. Posocco, P. et al. Interfacial tension of oil/water emulsions with mixed non-ionic surfactants: comparison between experiments and molecular simulations. *RSC Adv.* **6**, 4723–4729 (2016).
21. Owusu Apenten, R. K. & Zhu, Q.-H. Interfacial parameters for selected Spans and Tweens at the hydrocarbon–water interface. *Food Hydrocoll.* **10**, 27–30 (1996).
22. Byrnes, J. et al. Hemolysis during cardiac extracorporeal membrane oxygenation: a case-control comparison of roller pumps and centrifugal pumps in a pediatric population. *ASAIO J.* **57**, 456–461 (2011).
23. Omar, H. R. et al. Plasma free hemoglobin is an independent predictor of mortality among patients on extracorporeal membrane oxygenation support. *PLoS ONE* **10**, e0124034 (2015).
24. Dalton, H. J. et al. Factors associated with bleeding and thrombosis in children receiving extracorporeal membrane oxygenation. *Am. J. Respir. Crit. Care Med.* **196**, 762–771 (2017).
25. Valladolid, C., Yee, A. & Cruz, M. A. von Willebrand factor, free hemoglobin and thrombosis in ECMO. *Front. Med.* **5**, 228 (2018).
26. Wilson, A. M. M. et al. Hemolysis risk after packed red blood cells transfusion with infusion pumps. *Rev. Lat. Am. Enfermagem* **26**, e3053 (2018).
27. Prah, S. Optical absorption of hemoglobin. *Oregon Medical Laser Center* <https://omlc.org/spectra/hemoglobin/index.html> (1999).
28. Baskin, L., Dias, V., Chin, A., Abdullah, A. & Naugler, C. in *Accurate Results in the Clinical Laboratory* (eds Dasgupta, A. & Sepulveda, J. L.) 19–34 (Elsevier, 2013).
29. Jaouen, P., Vandanjon, L. & Quéméneur, F. The shear stress of microalgal cell suspensions (*Tetraselmis suecica*) in tangential flow filtration systems: the role of pumps. *Bioresour. Technol.* **68**, 149–154 (1999).
30. Kamaraju, H., Wetzel, K. & Kelly, W. J. Modeling shear-induced CHO cell damage in a rotary positive displacement pump. *Biotechnol. Prog.* **26**, 1606–1615 (2010).
31. Vázquez-Rey, M. & Lang, D. A. Aggregates in monoclonal antibody manufacturing processes. *Biotechnol. Bioeng.* **108**, 1494–1508 (2011).
32. Wang, S. et al. Shear contributions to cell culture performance and product recovery in ATF and TFF perfusion systems. *J. Biotechnol.* **246**, 52–60 (2017).
33. Nesta, D. et al. Aggregation from shear stress and surface interaction: molecule-specific or universal phenomenon? *Bioprocess Int.* **30**, 30–39 (2017).
34. Hejazian, M., Li, W. & Nguyen, N.-T. Lab on a chip for continuous-flow magnetic cell separation. *Lab Chip* **15**, 959–970 (2015).
35. Eijkel, J. C. T. & van den Berg, A. Nanofluidics: what is it and what can we expect from it? *Microfluid. Nanofluidics* **1**, 249–267 (2005).
36. Bocquet, L. & Charlaix, E. Nanofluidics, from bulk to interfaces. *Chem. Soc. Rev.* **39**, 1073–1095 (2010).
37. Bocquet, L. & Tabeling, P. Physics and technological aspects of nanofluidics. *Lab Chip* **14**, 3143–3158 (2014).

Publisher's note Springer Nature remains neutral with regard to jurisdictional claims in published maps and institutional affiliations.

© The Author(s), under exclusive licence to Springer Nature Limited 2020

Methods

Synthesis of rare-earth oil

Inspired by the well-known gadolinium complexes of DTPA, used as paramagnetic contrast agents in magnetic resonance imaging, we prepared an amphiphilic complex of DTPA with the paramagnetic rare-earth ion holmium(III), bearing two hydrophobic side chains connected to the DTPA moiety through ester linkage. In particular, by reaction of DTPA dianhydride with the branched alcohol 2-butyl-1-octanol we obtained a tricarboxylic chelating ligand, which on complexation with Ho^{3+} under alkaline conditions afforded a stable neutral Ho-DTPA complex. The latter, insoluble in water, was mixed with 2-butyl-1-octanol (30 wt% of the latter) affording a water-immiscible homogeneous fluid (Magoil) with positive magnetic susceptibility. The magnetic properties of the neutral Ho-DTPA complex (that is, before mixing with the alcohol) were evaluated by NMR measurement, using the Evans method³⁸, giving a value $4.40 \times 10^{-7} \text{ m}^3 \text{ mol}^{-1}$ for the molar susceptibility, which is comparable with that measured for the inorganic salt $\text{Ho}(\text{AcO})_3$, as well as of the order of magnitude expected for Ho^{3+} (ref. 39). Our paramagnetic oil is a transparent non-ionic liquid, slightly pink-yellowish because of the fluorescence of $\text{Ho}(\text{III})$, and it is physico-chemically stable in contact with aqueous solutions for several hours. Over longer periods of contact, hydrolysis occurs. Overall, these characteristics make it different from other magnetic fluids such as ferrofluids (black colloidal suspensions of nanometre-sized magnetic particles) or magnetic room-temperature ionic liquids. The preparation of the oil was easily scaled up to 25 g. We also used different trivalent rare-earth ions, such as erbium and terbium (Fig. 3b), obtaining analogous results.

Preparation of the $\text{Ho-DTPA-(2-butyl-1-octanol)}_2$ -based paramagnetic oil

DTPA dianhydride (5 g, 14 mmol) was dispersed in dry dimethylformamide (100 ml) under argon atmosphere, and the suspension obtained was heated to 70–75 °C under stirring, until complete solubilization was observed. After that, 2-butyl-1-octanol (5.5 g, 28 mmol, 2 eq.), dissolved in 10 ml DMF, was added dropwise to the above solution and the resulting homogeneous mixture was left under stirring at 50 °C for 4 h. The completeness of the reaction was monitored by liquid chromatography/mass spectrometry. Afterwards, the solvent was removed (rotary evaporation plus high-vacuum pump) to give **2** as a sticky yellowish solid that was used without further purification (Extended Data Fig. 2a).

To a stirred 0.2 M solution of the ligand **2** in ethanol (EtOH), an aqueous 1 M solution of NaOH (3 eq.) was added dropwise at room temperature, followed by the addition of $\text{HoCl}_3 \cdot (6\text{H}_2\text{O})$ (1.5 eq. with respect to **2**), dissolved in water to produce a final 0.1 M solution of the complex of **3** in ethanol:water 1:1. The resultant homogeneous mixture was left stirring at room temperature until a viscous pink oil, which responds to magnetic fields, separated out from the water phase (typically 0.5–1 h). After that, the solution was concentrated by rotary evaporation to remove EtOH, and the water phase was extracted with dichloromethane. The organic phase was separated, dried over MgSO_4 and rotary-evaporated to give the complex **3** as a glassy solid. Finally, the latter was dissolved in the minimum amount of dichloromethane, and the fatty alcohol 2-butyl-1-octanol (30 wt%) was added to the resultant solution. The mixture was then rotary-evaporated under high vacuum to eliminate dichloromethane, resulting in the target homogeneous transparent paramagnetic oil. The absorbance of the paramagnetic oil (Extended Data Fig. 2b) matches the absorption peaks of Ho^{3+} (ref. 40).

Measurement of the magnetic susceptibility of the paramagnetic oil

The magnetic susceptibility of the neutral complex **3** (Extended Data Fig. 2a) was measured by the Evans method, using NMR spectroscopy³⁸. This method relies on the fact that the chemical shift of the ^1H NMR signals of a molecule depend on the bulk susceptibility of the medium.

We used the resonance line of the residual proton of CDCl_3 (that is, the NMR solvent) as a reference, by comparing its chemical shift in pure CDCl_3 and in a CDCl_3 solution containing the complex **3**. From the difference in the chemical shifts we calculated the mass and molar susceptibilities of **3** ($\chi_{\text{mass}} = 4.88 \times 10^{-7} \text{ m}^3 \text{ kg}^{-1}$; $\chi_{\text{mol}} = 4.40 \times 10^{-7} \text{ m}^3 \text{ mol}^{-1}$).

Magnetic properties of the ferrofluids

Magnetization measurements were performed in a vibrating sample magnetometer with a compact variable permanent magnet source⁴¹. Samples were mounted in 3D-printed sample holders with cylindrical chambers of diameter 3 mm and length 3.88 mm or 5.88 mm, ensuring a well-defined demagnetization factor and maximal use of the uniform region of the pick-up coils.

The magnetic field dependence of the magnetization was assumed to be due to dispersed non-interacting spherical particles in a non-magnetic medium, and the data were fitted with either a single-component or two-component Langevin function. After correcting for non-zero magnetic field offsets, the applied field H was corrected for the appropriate demagnetization factor, N (ref. 42), to get the internal field H' . Additional magnetization measurements were performed by measuring the inductance of solenoids immersed in the ferrofluids. The solenoid inductance was measured using an LCR bridge meter (Hameg 8118) at 1 kHz. See Supplementary Information section I for Langevin and demagnetization factor equations.

Remanent magnetization of permanent magnets

The remanent magnetization M_r of the permanent magnets used was measured by profiling the external field with a Gaussmeter in the z direction along the central axis and fitting the resultant profile to analytical expressions⁴³ (see Supplementary Information section II for equations).

Magnetic field simulations

Assuming magnetically transparent, uniformly magnetized permanent magnets, 3D magnetic fields can be calculated with analytical expressions based on the surface charge model^{44,45}. The magnetic field at each point is summed over the contributions of each magnet in an assembly. Full expressions are presented in Supplementary Information section III.

Surface tension of magnetic liquids

A simple home-built pendent drop set-up was used to measure the surface tension of the magnetic liquids. The solutions were gradually dispensed in a stepwise fashion through a polished 74- μm -diameter glass capillary using a syringe pump into a glass cuvette in a 3D-printed support. The pendent drops were imaged using a Canon EOS 50D and Tamron superzoom 18–270-mm lens in RAW mode. RAW images were converted to monochrome TIFF files, with image processing being carried out in ImageJ⁴⁶, and the surface tension calculated using 'Pendent_Drop', an ImageJ plug-in⁴⁷.

The drops were gradually enlarged, with multiple images taken at each size until the drops broke off, and this was repeated at least six times. The values reported in Extended Data Table 1 are pooled mean and variance, calculated from at least six different droplets, for at least 15 droplet sizes, and three images per size. Overall, between 30 and 100 images of droplets of various sizes were used per surface tension value. Surface tension measurements were cross-checked with a Kruss Drop Shape Analyzer DSA100 and found to be in agreement.

Method for self-consistent diameter calculation with the full model

For a given set of conditions (that is, permanent magnet remanent magnetization, quadrupole spacing, ferrofluid nanoparticle diameter and volume fraction, and surface tension), d can be calculated in a self-consistent manner by calculating the magnetic field and magnetization at a position $d/2$ with the scheme in 'Remanent magnetization

Article

of permanent magnets', next generating a new d using equation (3), using this as a new input d , and looping repeatedly until the difference between input and output is negligible.

Side-view optical imaging and pressure/flow measurements

Images were acquired with either a Leica MZ16 stereo microscope with a Leica IC80HD digital camera, or a Nikon SMZ745T stereo microscope and a SONY colour CCD camera (1/1.8", 20 images per second, 1,600 × 1,200 pixels). An Elveflow OB1 pressure-driven pump and Elveflow FS4 flow sensors were used to set the applied pressure and measure the resulting flow rates in and out of the antitubes. All image processing and analysis was carried out in ImageJ⁴⁶. Image thresholding was performed using Otsu's clustering method, with the resulting image converted to a binary mask. Particle analysis and circle fitting was performed on each image, resulting in cross-sectional area, and roundness/circularity. Examples of cross-sections are shown in Extended Data Fig. 4d.

Optical transmission imaging

A Zeiss Axiovert 200M inverted microscope with a 5× NA = 0.15 objective and Andor Zyla 4.2 sCMOS detector were used to image through 3D-printed microfluidic devices. These devices consist of a main channel 200 μm high and 1 mm wide, a right-angled Y-junction for two water inlets, a ferrofluid inlet which joins the channel at its centre, a single outlet, and space to place four magnets to generate a quadrupolar field centred in the main channel. The device is sealed with a thin glass coverslip.

To stabilize antitubes, two methods were used. (i) The channel was prefilled with water, and the ferrofluid was injected, gradually displacing the water inside the channel; or (ii) the channel was prefilled with ferrofluid, with water injected to displace ferrofluid.

Tube diameter was estimated with ImageJ. Plot profiles were generated by taking column averages of images (Extended Data Fig. 3f, g), followed by subtraction of the background, leading to a sharp peak due to the lower absorption of water. This was fitted with a Gaussian peak function, whose full-width half-maximum (FWHM) corresponded to tube diameters measured from the optical side-view technique.

Top-view optical imaging through Magoil

A Nikon SMZ745T stereo microscope and a SONY colour CCD camera (1/1.8", 20 images per second, 1,600 × 1,200 pixels) were used to image water tubes inside Magoil. Similar to the X-ray and optical transmission images, the optical images were rotated and inverted (Extended Data Fig. 8), and profiles of column averages were extracted for data fitting. The background was subtracted, and the resulting peaks fitted with a Gaussian function.

X-ray transmission imaging

A MyRay dental X-ray imaging system was adapted for imaging through ferrofluids. It consisted of an X-ray source (MyRay RX-DC eXtend) and a detector (MyRay Zen X T1) purchased from Castebe (Waver, Belgium), and confined inside a box (constructed in-house) covered by lead plates. In general, X-ray emission at 65 kV and 6 mA with exposure time of 0.1 s was used to obtain a good-contrast image of water antitubes confined in ferrofluids.

To measure the tube diameter, first a background measurement was taken with a microfluidic device (Extended Data Fig. 3a, b) fully filled with ferrofluid. The image processing loop (also in ImageJ) consisted of taking the average of 10 images, rotated to have the tube fully vertical, with the intensity values inverted (Extended Data Fig. 3c). Next a plot profile was generated by taking column averages (Extended Data Fig. 3d, red line). Then a freshly cleaned device was filled with water, and ferrofluid was added progressively in 50 μl steps at a flow rate of 100 μl min⁻¹, with 10 images taken at each step. The same imaging process was carried out as with the background, followed by subtraction

of the background plot profile, leading to a sharp peak due to the lower absorption of water (Extended Data Fig. 3e). This was fitted with a Gaussian peak function, whose FWHM corresponded to tube diameters measured from the optical side-view technique. The procedure of adding ferrofluid was continued until a continuous tube was no longer observed. For improved contrast sensitivity, additional transmission images were taken with a Hamamatsu C7942CK-12 flat panel sensor in place of the MyRay Zen X T1 (Extended Data Fig. 1a, b).

Synchrotron X-ray tomography

Phase-contrast synchrotron X-ray tomography was carried out at the X02DA TOMCAT beamline of the Swiss Light Source (SLS) at the Paul Scherrer Institute. The X-ray beam, produced by a 2.9-T bending magnet on a 2.4-GeV storage ring (with ring current $I = 400$ mA), was monochromated to 30 keV. We used a high-speed CMOS (complementary metal-oxide-semiconductor) detector (PCO.Edge 5.5) coupled to a KinoOptik 1× visible-light objective with a 300-μm-thick LuAG:Ce scintillator, for a field of view 16.6 mm × 14.0 mm and effective pixel size 6.5 μm. The sample-to-detector distance was 327 mm. Raw images were acquired with 50-ms exposure times across 1,500 tomographic projections. Twenty dark and 100 flat-field images were collected for each scan.

The samples consisted of 3D-printed supports with circular cross-section and a 1.5-mm-diameter channel. There is a groove on the top and bottom of the holder to accommodate two N42 grade Nd₂Fe₁₄B magnets (10 × 10 × 10 mm) on each side at a distance of 3 mm. The 3D print is designed so that the centre of the null field is close to the centre of the fluidic channel. The channels were prefilled with water containing 1 vol% Tween-20 surfactant and imaged after sequential injection of known volumes of a ferrofluid with a syringe pump.

Before further analysis, each projection was corrected with the respective dark and flat-field image. Computed tomography reconstruction was performed with the 'gridrec' algorithm⁴⁸, enabling fast reconstructions of large datasets. Tomographic slices were rendered using ImageJ 1.52i, and the volumetric cross-sections were rendered using Paraview 5.6.0.

Antitube durability

The durability of the antitubes was tested by varying the flow rate of water with a syringe pump to determine the threshold value at which ferrofluid is sheared out. For this test, we used a fluidic chip that consists of four magnets (each 9 × 9 × 50 mm) with gaps of 9 mm between magnets. No major leakage of ferrofluid was observed throughout the measurement, and the threshold value was reported for the flow rate when iridescence due to a thin film of oil on the water surface was observed. The observed data (Extended Data Fig. 4a, b) are valid only for this specific magnet arrangement and fluidic circuit, as the magnetic field distribution varies when the size and arrangement of magnets are changed, and outlets perpendicular to the main channel inhibit further leakage. In general, the threshold value increases when more viscous or magnetically stronger ferrofluids are used for antitube formation and decreases as the antitube diameter decreases.

Quantitative analysis of water contamination by magnetic media

The amount of magnetic media leaked into water was quantified by atomic absorption spectroscopy (AAS; Agilent Technologies 200 Series AA). The emission wavelengths of iron (372 nm) and holmium (559 nm) were used for ferrofluids and Magoil, respectively. The standard samples for iron were prepared by dissolving iron metal in hydrochloric acid and diluted by distilled water to obtain a series of concentrations to construct a calibration curve. Each point is from five consecutive measurements. We mixed 1 ml of ferrofluid (MKC and MD4) and 25 ml of distilled water in a separatory funnel and left them overnight. We then transferred 20 ml of the distilled water from the funnel to a vial and removed water by using

a rotary evaporator. Hydrochloric acid (1 ml) was added to the vial to dissolve any remaining iron. The iron solution was diluted to make 50 ml in total and used for AAS. Similarly, we mixed 1 ml of Magoil with 25 ml of distilled water. Five consecutive measurements were performed for each sample to build the statistics. Emission intensities of 0.049 ± 0.002 and 0.050 ± 0.004 were observed from the water samples in contact with MKC and MD4, respectively. Using the calibration curve and error propagation analysis, the concentration of the iron from water in contact with MKC and MD4 was determined as 0.78 ± 0.05 ppm and 0.79 ± 0.08 ppm.

Additional checks were made by flowing water through antitubes of three different diameters, 3.5 mm, 1.5 mm and 0.8 mm. The cavity containing both ferrofluid and water was 6 mm in diameter. We used DI water as transported fluid. The surrounding ferrofluid was APG1141 with viscosity 5 Pa s. Three flow rates were used, corresponding to 10%, 50% and 75–80% of the threshold flow rate for each diameter ($Q_{\text{thres}} = 80 \text{ ml min}^{-1}$, 60 ml min^{-1} and 30 ml min^{-1} , respectively; see Extended Data Fig. 4a, b). The set-up consists of a pressure-driven pump (Elvesys OB1) connected to a water reservoir which is then connected to the antitube housed in a 3D-printed support. At the outlet, the flow is split into two streams. One passes directly to a tube, and the other flows adjacent to a magnet ($6 \times 6 \times 50 \text{ mm}$) before entering a second tube. This additional magnet was placed with its long axis parallel to the channel flow and is there to capture any ferrofluid that may inadvertently shear out under flow. The water was flowed continuously for 1.5 h, and 45-ml samples were collected in each Falcon tube at the beginning, middle and end of the experiment. All solutions were evaporated, followed by the addition of 1 ml concentrated HCl, which was allowed to react for 1 h and diluted with 45 ml of ultrapure H_2O . The entire procedure was repeated to produce a total of six samples per experimental condition, with the data reported in Extended Data Fig. 4f being the average values, and error bars being the standard deviations. Here we found that all Fe concentrations detected were below 0.3 ppm, with most of them within one standard deviation for a series of blank measurements.

Magoil hydrolyses in a few hours, and therefore 20 ml of water was transferred to a vial after one hour and diluted to make a total 50 ml of the sample for AAS. Holmium(III) chloride was dissolved in distilled water and diluted to obtain a calibration curve. The emission intensity of 0.058 ± 0.001 was observed from the water sample that was in contact with Magoil, which corresponds to 2.6 ± 0.1 ppm based on the calibration curve.

Construction of Qpump

The Qpump housing was 3D-printed using F170 (Stratasys) with ABS (acrylonitrile butadiene styrene)-M30. $\text{Nd}_2\text{Fe}_{14}\text{B}$ arc magnets were purchased from NEOTEXX (TR-036.5-33-20-NN and -SN, TR-028.5-25-20-NN and -SN). A high-power gear motor (RobotShop, Devantech 24V) was used to rotate the inner rotor of the Qpump. The fluidic chips were 3D-printed using a Form 2 print (Formlabs) with a clear resin (FLG-PCL02). The chips were then connected to Tygon tubing (Saint-Gobain, ND 100-65, 1/16" inner diameter (ID) \times 1/8" outer diameter (OD)).

Blood pumping and analysis

Human blood (50 ml) from a unique donor at l'Établissement français du sang (EFS) Strasbourg was used for each set of experiments. The blood was collected on anticoagulant with hirudin ($100 \text{ units ml}^{-1}$). Six 6-ml tubes were prepared for each experiment: one as a negative control (not used in a pump), three for use with a Qpump, and two for a peristaltic pump. To build statistics, blood from three different donors was used to construct the data reported here. The rotation rate of motors was adjusted to obtain the flow rate of each pump at -1.5 ml min^{-1} . Tygon tube (Saint-Gobain, Tygon 3350, 1/16" ID \times 3/16" OD) with stoppers was used with the peristaltic pump (Fischer Scientific, CTP300).

After an hour of blood pumping in a closed circuit (Fig. 4a), the whole blood from each tube was analysed with a haematology analyser (Sysmex Europe, XN-1000). Then the whole blood was centrifuged (SORVALL RC3BP, 10 min at 250 g, room temperature) to obtain PRP

for UV-vis spectroscopy (Agilent, Cary 8454) and light transmission aggregometry (APACT 4004). For UV-vis spectroscopy, PRP was 25 times diluted with phosphate buffer. Light transmission was recorded during 5 min while platelets aggregated after the addition of $30 \mu\text{l}$ of agonist (TRAP $10 \mu\text{M}$) into $270 \mu\text{l}$ of PRP.

To perform electron microscopy imaging of platelets, samples were prepared as follows: first, $100 \mu\text{l}$ of PRP was added to $400 \mu\text{l}$ glutaraldehyde 2.5% (Euromedex, I6210) in cacodylate (CACO) buffer in a 15-ml tube and incubated overnight at 4°C . Then the solution was centrifuged for 8 min at $2,000g$ to obtain pellet platelets, which were then resuspended with 2 ml CACO buffer for washing. This solution was centrifuged again for 8 min at $2,000g$, and the collected platelets were resuspended with $250 \mu\text{l}$ of CACO buffer. Finally, the solution was diluted 10 times, and $100 \mu\text{l}$ of diluted solution was deposited on a poly-L-lysine (Sigma Aldrich, P8920) coverslip (Euromedex, 72226-01) to sediment the platelets at room temperature. After 30 min, the excess solution was removed, and the substrate was washed twice with CACO buffer for 5 min. Dehydration of the substrate was done with ethanol (LPCR (Les Produits Chimiques de la Robertsau) 20821296): 70% ($3 \times 5 \text{ min}$), 85% (5 min), 95% (5 min) and 100% ($2 \times 30 \text{ min}$). The substrate was then desiccated with hexamethyldisilazane (LPCR, I12186.0100): 1/4 HMDS + 3/4 ethanol 100% (5 min), 1/2 HMDS + 1/2 ethanol 100% (5 min), 3/4 HMDS + 1/4 ethanol 100% (5 min) and pure HMDS ($2 \times 5 \text{ min}$). The coverslip was fixed on an aluminium support mount (Euromedex, 75230) with conductive carbon cement (Euromedex, I2664). The sample was metallized (coating by -10-nm layer of platinum and palladium) by a Cressington 208 HR sputter coater and observed with Phenom Pro Desktop SEM for high-quality imaging.

Ferrofluid contamination in the pumped blood was determined using the protocol in 'Quantitative analysis of water contamination by magnetic media', along with a complementary method of measuring the magnetic moment of the whole blood samples in a SQUID magnetometer (Quantum Design MPMS3 SQUID-VSM). First, the ferrofluid MKC was dried by rotary evaporation to measure the magnetic response without the hydrocarbon carrier fluid. Similar to the Langevin function fitting (see 'Magnetic properties of the ferrofluids'), the concentration of superparamagnetic magnetite nanoparticles in the powder was found to be 76%.

Next, eight whole-blood samples, four pumped through two different Qpumps, two pumped through a peristaltic pump, and two controls (not pumped at all), were lyophilized before mounting in gelatine capsules. The control and peristaltic pumped samples showed only a diamagnetic susceptibility at room temperature, as expected for oxyhaemoglobin, with an average susceptibility of $-2.3 \pm 0.3 \text{ A m}^2 \text{ kg}^{-1} \text{ T}^{-1}$ (after correction for sample holder contributions). In these blood samples, deoxyhaemoglobin is visible only at low temperatures, where a Brillouin function fit reveals an average of four unpaired spins, as expected. In contrast, the four magnetically pumped samples returned an average superparamagnetic moment of $26.2 \pm 14.8 \times 10^{-3} \text{ A m}^2 \text{ kg}^{-1}$, which is the equivalent of 285 ± 161 ppm of Fe_3O_4 per gram of blood.

Derivation of equations (1) and (2)

We use the steady-state Stokes equations in radial coordinate for ferrofluid as well as honey. The fluid landscape is divided into three regions, namely the honey flow (region I), ferrofluid with shear flow (region II) and reverse flow of ferrofluid (region III) (see Extended Data Fig. 5e). The solid walls are given a zero-velocity boundary condition, and the interface between the liquids has continuous velocity and shear stress. As there is no net flow of ferrofluid, the flow rate of ferrofluid in region III is equal and opposite to that in region II. This can be seen in the normalized velocity profile in Extended Data Fig. 4e which was also confirmed by numerically solving the Navier–Stokes equation in Extended Data Fig. 5a–d. Finally, solving the Stokes equations with the respective boundary conditions, the effective slip length is defined in terms of the flow rate (for a fixed pressure gradient) in the system. The full derivation is presented in Supplementary Information section III.

Derivation of equilibrium diameter equation (3)

The approach starts with the magnetically augmented Bernoulli equation, choosing appropriate boundary conditions at two points (see Extended Data Fig. 5f), one at the centre of the antitube in the null field region, P_1 , and the other at the boundary between the inner solution and the magnetic liquid, P_2 , and solving the Bernoulli equation to arrive at an expression due to the balance of energies at the interface. A derivation is provided in Supplementary Information section IV.

Derivation of linear and saturation models for equilibrium tube diameter

Equation (3) is simplified to equation (4) by linearizing the magnetic field dependence inside the quadrupole, assuming a linear magnetic susceptibility for the ferrofluid, and inserting both results into equation (3). A full derivation is described in Supplementary Information section V.

Computational fluid dynamics

Finite element methods using ANSYS 18 were used to simulate fluid dynamics of a honey antitube inside EMG900 ferrofluid. A full 3D simulation was performed, with the following boundary conditions applied: at the inlet we define the flow rate ($Q = 175 \mu\text{l min}^{-1}$), and the outlet is set to atmospheric pressure. The interface between liquids is defined as two walls with constant magnitude of shear stress (τ). We vary the shear stress until the velocity at the interface becomes continuous. Once the shear stress and velocity become continuous, the solution is accepted. Here $\tau = 0.45 \text{ Pa}$ for the semi-infinite case and $\tau = 0.47 \text{ Pa}$ for the case in which we include the effect of curved inlet and outlet. The reverse flow as predicted by the analytical model is clearly seen in the simulations. The antitube diameter is 1.2 mm and the cavity size is 4.4 mm. The fluids used are honey with viscosity 10 Pa s and EMG900 (ferrofluid) with viscosity 0.06 Pa s. To simplify the simulations, we use free slip conditions at the curved inlet and outlet region. This is because the change in the velocity in the curved inlet and outlet region is dominated solely by the change in diameter.

When comparing an infinite channel (Extended Data Fig. 5a, b) to a finite channel (Extended Data Fig. 5c, d), we observe the same counterflow of ferrofluid. For the finite channel, the velocity away from either the inlet or outlet has a flat, plug-like profile (Extended Data Fig. 5d) identical to the infinite channel (Extended Data Fig. 5b), but at the outlet there is a large drop in the flow velocity as the volumetric flow rate is fixed and the channel widens. Furthermore, most of the pressure drop occurs at both the inlet and outlet where the channel diameter changes (Extended Data Fig. 5c). Additionally, we observe the same pressure drop inside the finite antitube away from the inlet and outlet, as found for the infinite antitube (Extended Data Fig. 5a).

Reporting summary

Further information on research design is available in the Nature Research Reporting Summary linked to this paper.

Data availability

Source data for Figs. 2, 3 and 4 (and Extended Data figures containing data graphs) are provided with the paper. Any other data that support

the findings of this study are available on the Zenodo data repository, <https://doi.org/10.5281/zenodo.3603029>

Code availability

The Python code for calculating magnetic fields is available on the Zenodo data repository, <https://doi.org/10.5281/zenodo.3603029>

38. Evans, D. F. The determination of the paramagnetic susceptibility of substances in solution by nuclear magnetic resonance. *J. Chem. Soc.* **1959**, 2003–2005 (1959).
39. Coey, J. M. D. *Magnetism and Magnetic Materials* (Cambridge Univ. Press, 2010).
40. Sastri, V. R., Perumareddi, J. R., Rao, V. R., Rayudu, G. V. S. & Bünzli, J.-C. G. *Modern Aspects of Rare Earths and their Complexes* (Elsevier, 2003).
41. Cugat, O., Byrne, R., McCaulay, J. & Coey, J. M. D. A compact vibrating-sample magnetometer with variable permanent magnet flux source. *Rev. Sci. Instrum.* **65**, 3570–3573 (1994).
42. Wysin, G. M. *Demagnetization Fields* (Kansas State Univ., 2012); <https://www.phys.k-state.edu/personal/wysin/notes/demag.pdf>.
43. Furlani, E. P. *Permanent Magnet and Electromechanical Devices* (Academic, 2001).
44. Yang, Z. J., Johansen, T. H., Bratsberg, H., Helgesen, G. & Skjeltorp, A. T. Potential and force between a magnet and a bulk $\text{Y}_1\text{Ba}_x\text{Cu}_3\text{O}_{7-x}$ superconductor studied by a mechanical pendulum. *Supercond. Sci. Technol.* **3**, 591 (1990).
45. Camacho, J. M. & Sosa, V. Alternative method to calculate the magnetic field of permanent magnets with azimuthal symmetry. *Rev. Mex. Fis. E* **59**, 8–17 (2013).
46. Schindelin, J. et al. Fiji: an open-source platform for biological-image analysis. *Nat. Methods* **9**, 676–682 (2012).
47. Daerr, A. & Mogne, A. Pendent_Drop: An ImageJ plugin to measure the surface tension from an image of a pendent drop. *J. Open Res. Softw.* **4**, e3 (2016).
48. Marone, F. & Stamparoni, M. Regridding reconstruction algorithm for real-time tomographic imaging. *J. Synchrotron Radiat.* **19**, 1029–1037 (2012).

Acknowledgements We acknowledge the support of the University of Strasbourg Institute for Advanced Studies (USIAS) Fellowship, the 'Chaire Gutenberg' of the Région Alsace (J.M.D.C.), the French National Research Agency (ANR) through the Programme d'Investissement d'Avenir under contract ANR-11-LABX-0058_NIE within the Investissement d'Avenir programme ANR-10-IDEX-0002-02, and SATT Conectus funding. This project has received funding from the European Union's Horizon 2020 research and innovation programme under the Marie Skłodowska-Curie grant agreement no. 766007. We acknowledge the Paul Scherrer Institut for provision of synchrotron radiation beamtime at beamline TOMCAT of the SLS. We thank H. Boping of San Huan Corporation for giving us thin magnetic bilayer sheets. We thank F. Chevrier for technical support, and the staff of the STnano nanofabrication facility for help in sample fabrication. We thank N. Matoussevitch for the synthesis of ferrofluids. We thank F. Sacarelli and G. Formon for additional AAS measurements, A. Cebers of the University of Latvia Riga for the use of ANSYS 18, and S. Potier for advice on the project.

Author contributions J.M.D.C., B.D. and T.M.H. conceived and initiated the project. T.A. and P.D. performed most of the experiments and modelling. T.A., J.M.D.C., B.D., P.D. and T.M.H. designed the microfluidics set-ups. A.A.D. performed slip length experiments and modelling. P.D. carried out the magnetic modelling. A.S. developed and synthesized Magoil. L.G. characterized liquid and pumping properties. A.B. led the X-ray tomography experiments. T.A., C.B., T.M.H. and P.H.M. designed and conducted the blood experiments. T.A., J.M.D.C., B.D., P.D. and T.M.H. drafted the manuscript. All authors discussed and contributed to the paper in its final form.

Competing interests T.M.H. holds shares in Qfluidics, a company devoted to the commercialization of the liquid tube technology presented in this work. P.D., B.D., J.M.D.C. and T.M.H. are co-inventors on patents protecting the technology (WO2018134360A1, pending) for which all parts of the manuscripts are covered.

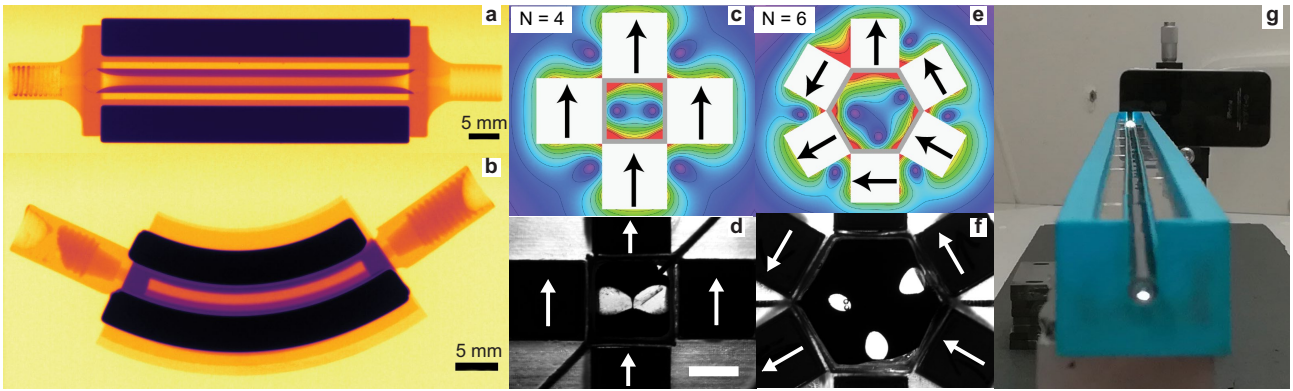
Additional information

Supplementary information is available for this paper at <https://doi.org/10.1038/s41586-020-2254-4>.

Correspondence and requests for materials should be addressed to T.M.H.

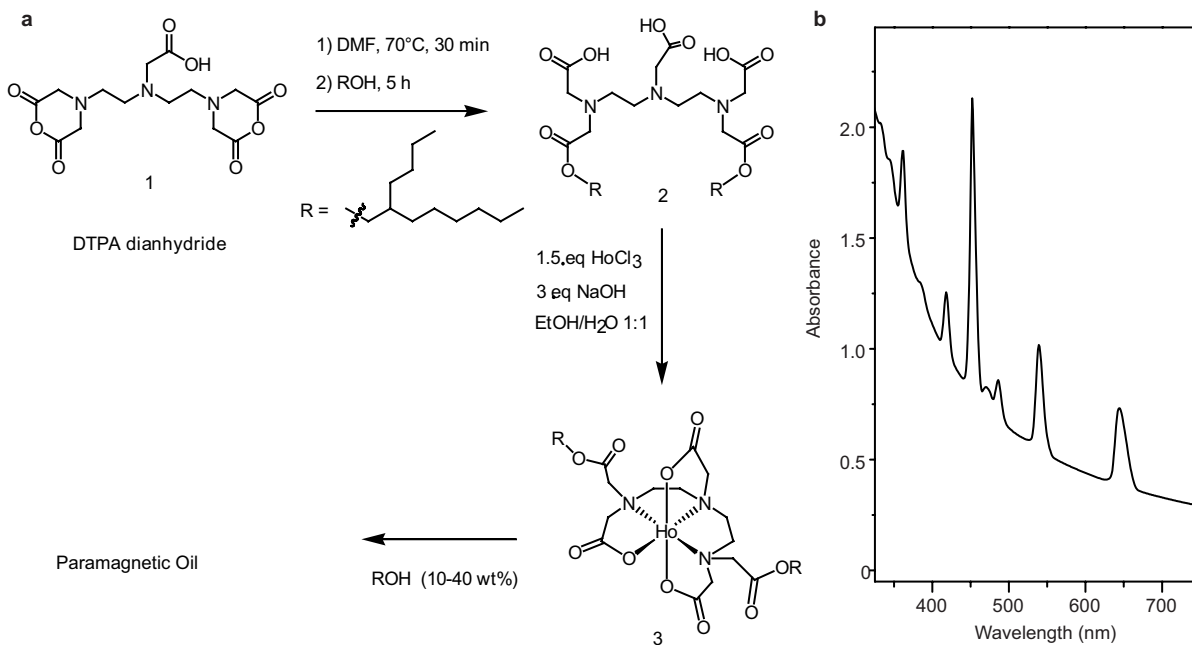
Peer review information Nature thanks Emmanuel Delamarque and the other, anonymous, reviewer(s) for their contribution to the peer review of this work.

Reprints and permissions information is available at <http://www.nature.com/reprints>.

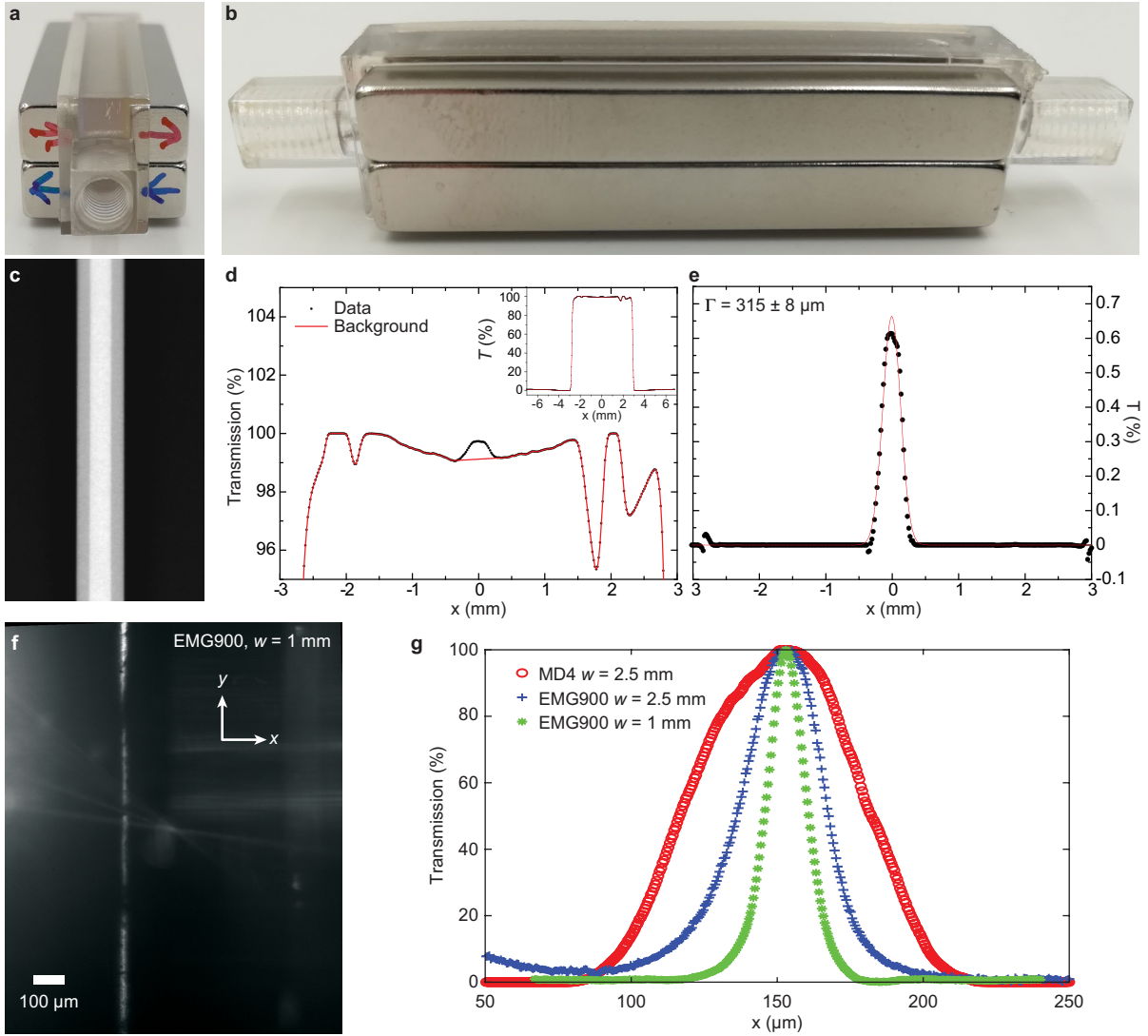


Extended Data Fig. 1 | Adaptability of antitube topologies to arbitrary magnetic fields. **a, b**, X-ray transmission images of an antitube of water inside a ferrofluid for cuboid magnets ($6 \times 6 \times 50$ mm) with 6-mm gap (**a**); and matching arc magnets of height 20 mm, 3.5-mm gap, and inner and outer diameter pairs of: ID 25 mm, OD 28.5 mm; and ID 33 mm, OD 36.5 mm (**b**). **c-f**, Antitube cross-sections using non-quadrupolar fields: the magnetic field

calculation (**c**) and experimental cross-section (**d**) for a four-magnet arrangement; and the magnetic field calculation (**e**) and experimental cross-section (**f**) for a six-magnet arrangement. Scale bar, 3 mm. See Supplementary Videos 5, 6. **g**, Side view of a 1-m-long water antitube ($d = 2$ mm), which allows light to pass throughout, showing the continuous water phase.

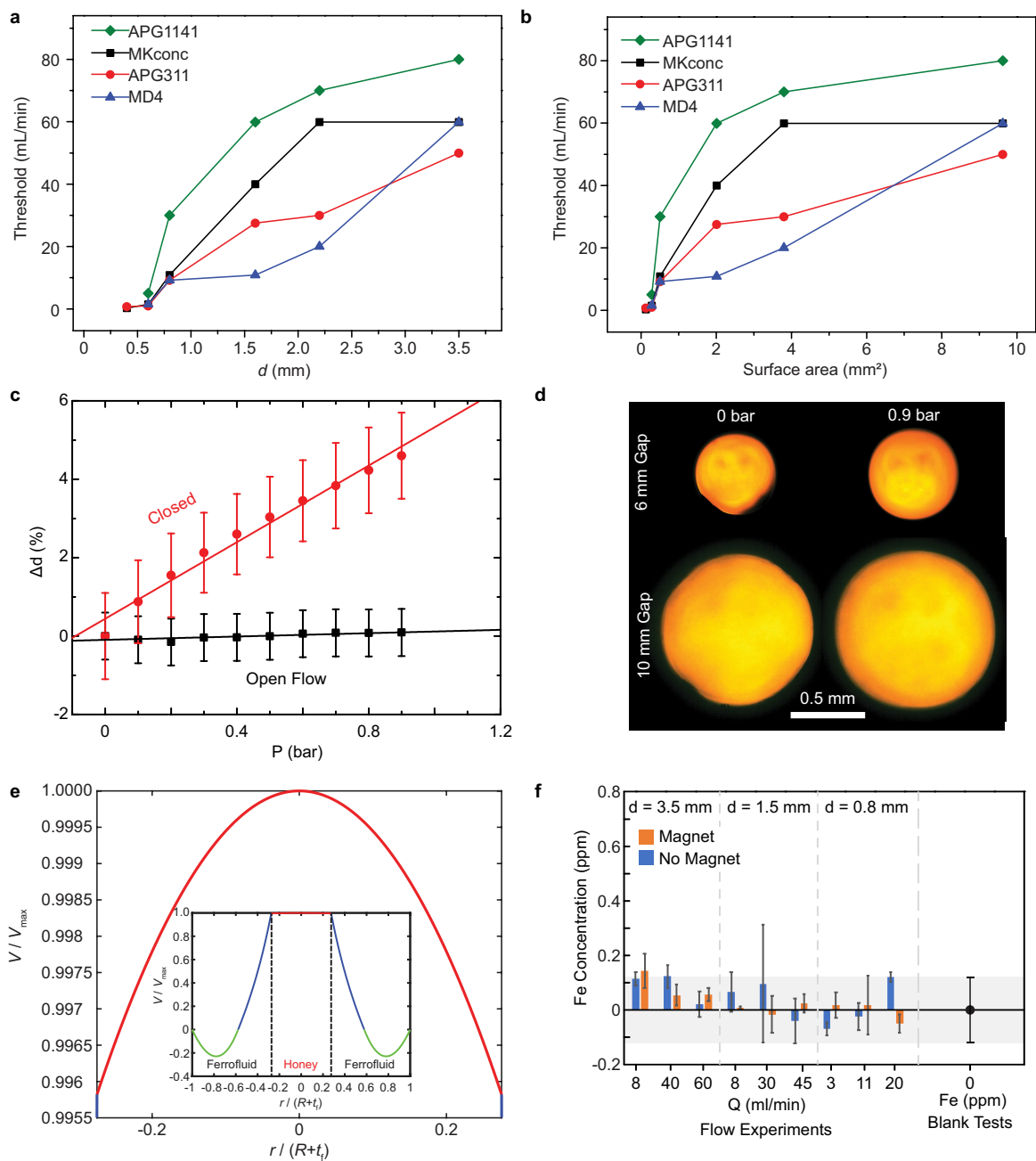


Extended Data Fig. 2 | Magoil synthesis and optical absorption properties. **a**, Magoil synthesis reaction scheme. DMF, dimethylformamide; EtOH, ethanol. **b**, UV-vis absorption spectrum of Ho³⁺-based paramagnetic Magoil.



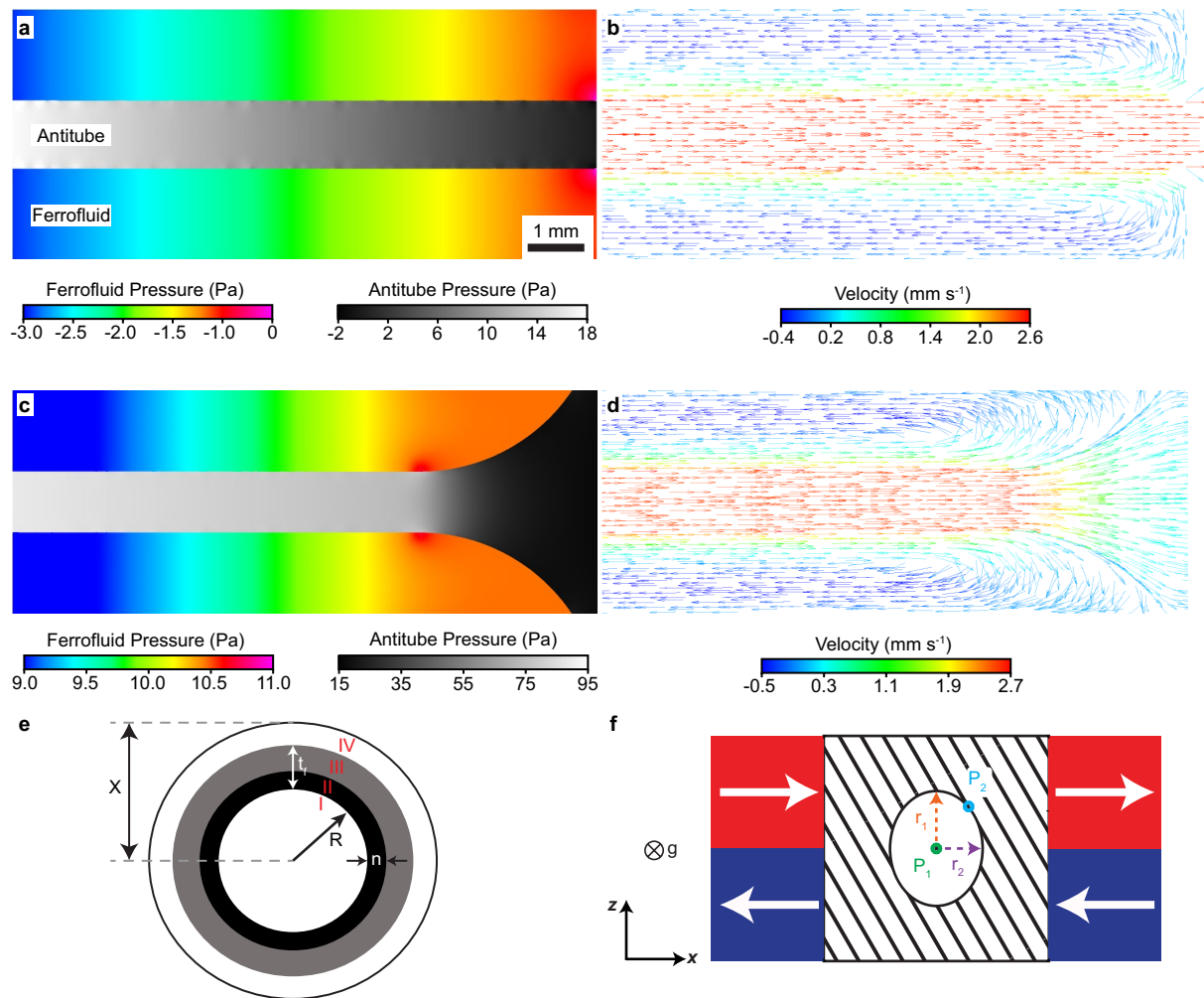
Extended Data Fig. 3 | Process steps involved in X-ray and optical imaging of antitubes in ferrofluids. **a, b**, Typical quadrupole assemblies used for X-ray measurements. **c**, Inverted transmission X-ray image. **d**, Transmission averaged along the channel. **e**, Background-corrected transmission through the water

antitube fitted with a Gaussian peak function. **f**, Optical image of a sub-100- μm water antitube in an EMG900 ferrofluid (double surfactant). **g**, Intensity profile across the microfluidic channel in the vicinity of the water antitube. The profile is column-averaged along the length of microfluidic channel.



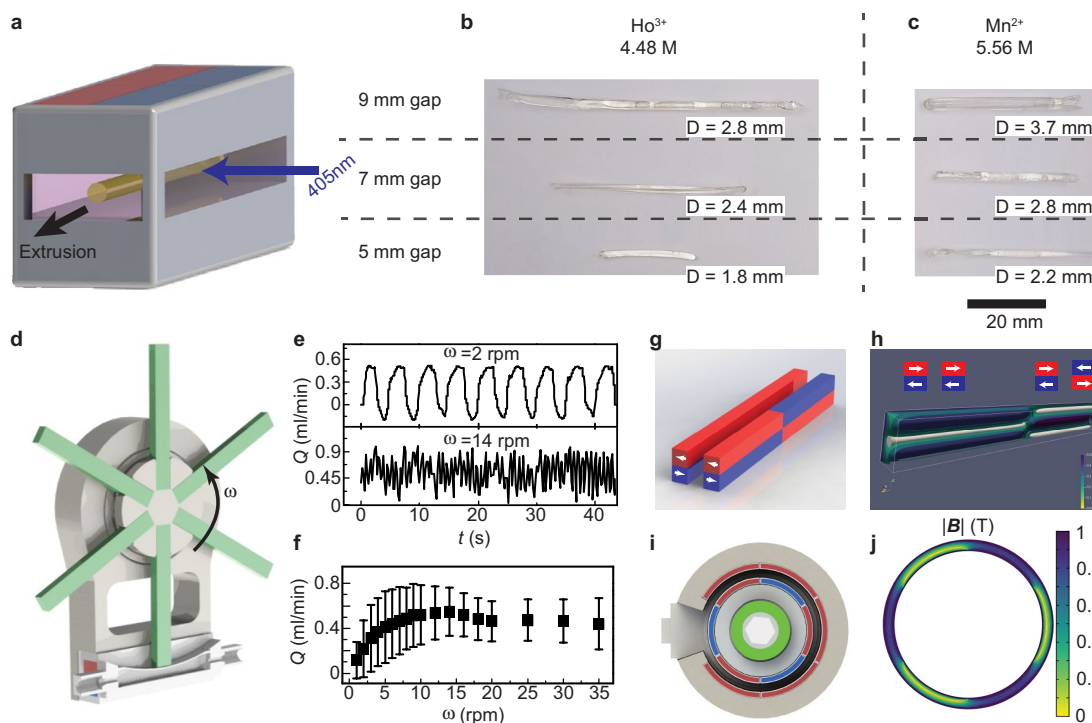
Extended Data Fig. 4 | Antitube stability and shear resistance under flow.
a, b, The threshold flow rate for antitube diameters **(a)** and areas **(b)**. **c**, Relative dilation of an antitube in APG311 ferrofluid with a quadrupolar gap, w , of 10 mm under flow and with the outlet closed. **d**, Side view through the antitubes under static conditions with no flow (outlet closed) for two magnet gaps at equilibrium (0 bar) and under 0.9-bar pressure. **e**, Normalized velocity profile

inside honey using equations (1) and (2), corresponding to data in Fig. 2d. Inset shows velocity profile in both honey and ferrofluid. **f**, Concentration of Fe found in water after pumping through three different antitube diameters for three flow rates with and without an extra magnet on the outlet flow. Blank tests for pure water give the grey background threshold detection. Values are averages of six samples, error bars are standard deviations.



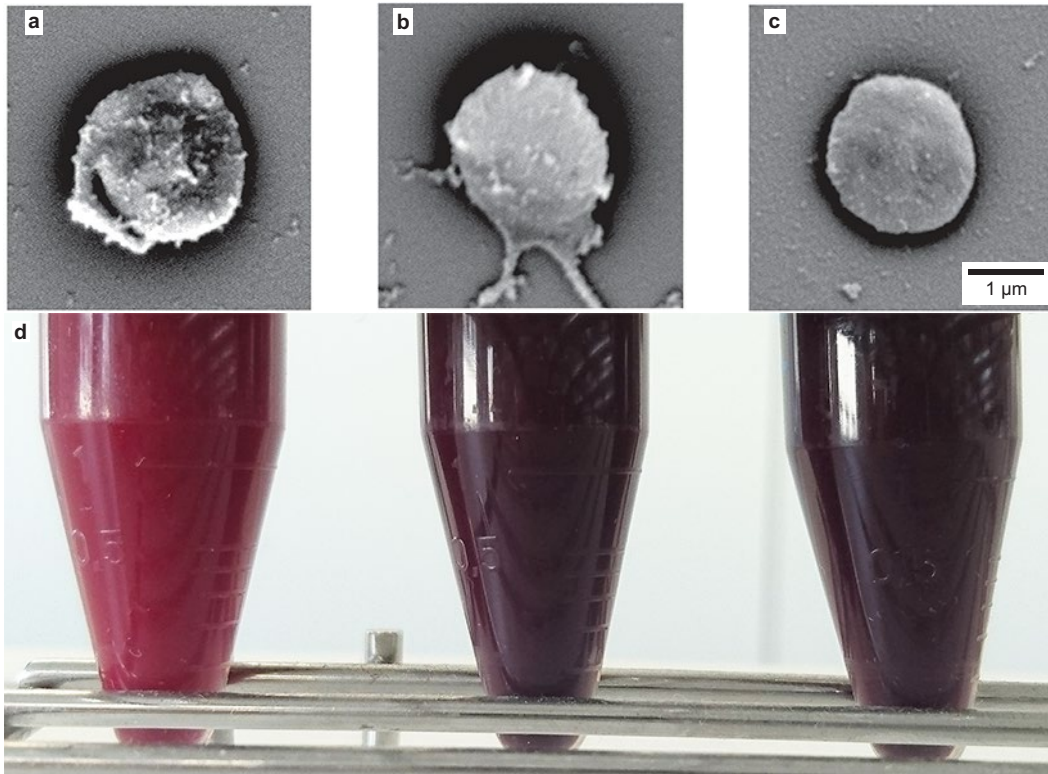
Extended Data Fig. 5 | Flows in antitubes and surrounding ferrofluid using computational fluid dynamics. **a–d**, Contour plots from numerical simulations of a honey antitube in EMC900 ferrofluid under a flow rate of $175 \mu\text{l min}^{-1}$ for two cases: first, the semi-infinite case with no inlet effects (**a, b**); second, the finite case including inlet effects with the ferrofluid contours matching those found by experiment (**c, d**) (compare with Extended Data Fig. 1a). The plots are (**a, c**) isometric pressure contours for at the outlets; note the different colourmaps for the pressure inside the ferrofluid versus inside the antitube; (**b, d**) velocity vector field at the outlets. **e, f**, Geometries used in the derivation of equations (1)–(4). **e**, Cross-section of liquid tube system considered in derivation of equilibrium diameter equation (3) (see Methods),

with four different flow regions consisting of: I, honey; II, a parallel flow of ferrofluid; III, a counterflow of ferrofluid; and IV, a fictitious region to define the radial distance x at which the flow velocity becomes zero. Thus, the slip length for a flow of honey is $b = x - R$, where t_i is the thickness of the ferrofluid, n is the thickness of region with shear flow and R is the radius of the honey tube. **f**, 2D geometry of four bar magnets in a quadrupolar configuration considered in the derivation of linear and saturation models for the equilibrium tube diameter (see Methods and Supplementary Information). The hatched region denotes the ferrofluid, and the white region in the centre is the contained liquid tube.



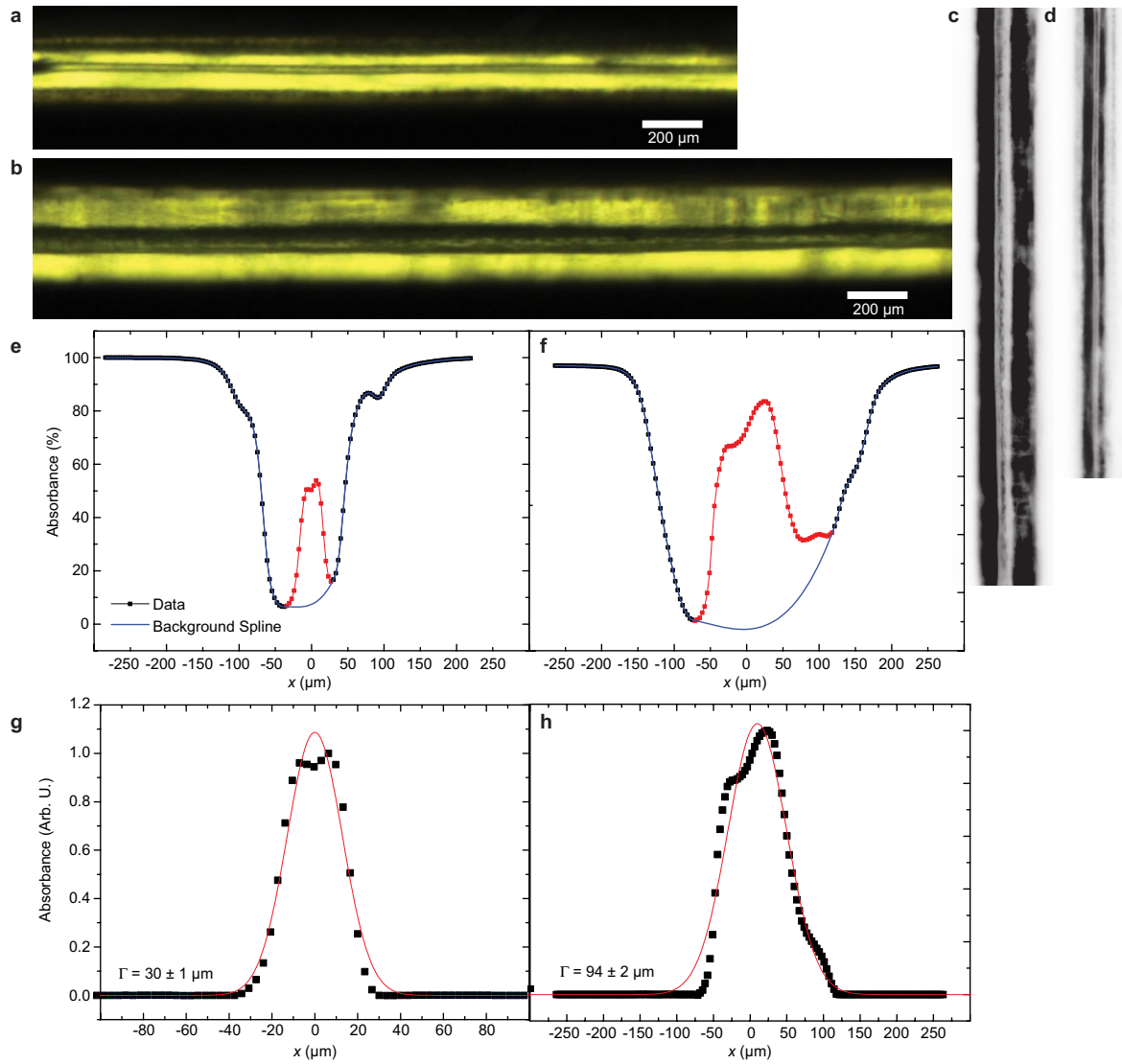
Extended Data Fig. 6 | Demonstration of photo-polymerization and pumping functionality in antitubes. **a**, A scheme of the fluidic chip used for the extrusion of a photopolymer resin and its photopolymerization by 405-nm laser light during extrusion. **b, c**, Photos of polymerized tubes extruded in **(b)** an aqueous HoCl_3 solution, and **(c)** an aqueous MnCl_2 solution. The diameter of the tubes decreased as the magnet gap decreased, and those photopolymerized in Ho^{3+} were smaller, as Ho^{3+} has higher magnetic susceptibility than Mn^{2+} . **d**, Isometric-view of a six-spoke magnetostatic pump (see Supplementary Video 11). **e**, Slow rotation (2 rpm) leads to pulsed flow, whereas fast rotation (14 rpm) produces a smoother flow. **f**, The average flow rate and standard deviation versus rotation rate ω . **g**, The magnetic

configuration for an antitube (section nearer the viewer) and a pinching region (further section) using magnets ($6 \times 6 \times 50$ mm) with a gap of 6 mm. **h**, Isosurface plot of the calculated magnetic field for **g**. The weak field region where water can reside is highlighted in white. A water antitube created by the quadrupolar arrangement (left half) is disrupted at the interface between two regions. The field created by the pinching geometry has a field strength of 0.5 T at the centre of magnets (represented by the dark blue colour). **i**, Top view of the Qpump based on this principle. The orientation of magnetization for the arc segments is radially outward (red) or inward (blue). **j**, x - y contour plot of the calculated magnetic field along the z -axis centre of the Qpump.



Extended Data Fig. 7 | Comparison of platelet and whole blood quality in peristaltic and magnetostatic pumping. **a - c.** Representative SEM images of platelets: after peristaltic pumping (**a**); platelets from control blood (**b**); and platelets from blood after Qpump pumping (**c**). No major morphological

change due to the activation of platelets was observed for either type of pump (peristaltic or Qpump). **d.** A picture of the whole blood in a tube after peristaltic pumping (left), control (middle) and Qpump pumping (right).



Extended Data Fig. 8 | Process steps for optical imaging of antitubes in Magoil. **a, b**, Optical micrographs of a water antitube in Magoil for a gap width $w = 220 \mu\text{m}$ (**a**) and $w = 307 \mu\text{m}$ (**b**). **c, d**, Greyscale, rotated and inverted images for **b** and **a** respectively. **e, f**, Column average profiles of gap for **a** and **b**, respectively. **g, h**, Gaussian function fits to the background subtracted

profiles. Note: the $94\text{-}\mu\text{m}$ antitube is thermodynamically stable, as the image was taken during the extrusion of the water antitube, whereas the $30\text{-}\mu\text{m}$ tube is thermodynamically unstable. After injection, water was then extracted, resulting in a thinning of the tube, which at this diameter collapses into droplets in a matter of minutes.

Extended Data Table 1 | Physical properties of magnetic liquids used

Sample	ρ kg m ⁻³	d_1 nm	d_2 nm	ϕ_1 %	ϕ_2 %	χ	σ_{air} mN m ⁻¹	σ_{water} mN m ⁻¹	σ_{tween} mN m ⁻¹
APG 311	950 ± 50	8.2 ± 0.03	–	2.2 ± 4.10 ⁻³	–	0.151 ± 0.001	24.7 ± 0.8	22.8 ± 0.8	5.9 ± 0.6
EMG 900	1720 ± 90	11.3 ± 0.1	5 ± 0.1	9.2 ± 0.1	3.3 ± 0.1	1.67 ± 0.04	22 ± 0.5	29.2 ± 1.4	7 ± 0.3
Magoil	970 ± 50	–	–	–	–	4.7 × 10 ⁻⁴ ± 0.5 × 10 ⁻⁴	–	5.8 ± 0.4	–

Measured physical properties of the two commercial ferrofluids (APG311 and EMG900; Ferrotec) and paramagnetic oil (Magoil): density ρ , nanoparticle diameters d_1 and d_2 (for bimodal size distributions), corresponding volume fractions ϕ_1 and ϕ_2 of magnetite in the suspension, initial susceptibility χ , surface tension σ with air, surface tension with water, and surface tension with 1% Tween-20 in water.

Article

Extended Data Table 2 | Cell counts of whole blood

	RBC	HGB	HCT	MCV	MCH	MCHC	RDW-SD	RDW-CV	PLT&F	PDW	MPV	P-LCR	PCT	IPF	WBC
unit	10 ⁶ /μL	g/dL	%	fL	Pg	g/dL	fL	%	10 ³ /μL	fL	fL	%	%	%	10 ³ /μL
ctrl	4.07	12.3	35.5	87.2	30.2	34.6	42.8	13.2	203	11.6	10.5	28.2	0.21	3.3	3.58
Qpump 1	4.11	12.3	35.7	86.9	29.9	34.5	42.1	13.2	169	10.8	10.2	26.8	0.17	3.3	3.44
Qpump 2	3.99	12	34.7	87	30.1	34.6	41.4	13.1	159	11.4	10.5	26.9	0.17	3.3	3.46
Peristaltic pump 1	3.56	10.7	30.4	85.4	30.1	35.2	40.6	13.1	192	11.9	10.7	29	0.22	4.2	3.84
Peristaltic pump 2	4.06	12.3	34.7	85.5											

Comparing a control experiment, after pumping by Qpump, and after peristaltic pumping, measured by haematology analyser (Sysmex XN-1000). Each set of experiments was performed using blood from the same donor. RBC, red blood cells; HGB, haemoglobin; HCT, haematocrit (volume percentage of RBC); MCV, mean corpuscular volume (average RBC volume); MCH, mean corpuscular haemoglobin (average quantity of haemoglobin per RBC); MCHC, mean corpuscular haemoglobin concentration; RDW, RBC distribution width (-SD for standard deviation, -CV for coefficient of variation); PLT&F, platelet counts by fluorescence analysis; PDW, platelet distribution width; MPV, mean platelet volume; P-LCR, platelet large cell ratio; PCT, plateletcrit (volume percentage of platelets in the blood); IPF, immature platelet fraction; WBC, white blood cells.

Reporting Summary

Nature Research wishes to improve the reproducibility of the work that we publish. This form provides structure for consistency and transparency in reporting. For further information on Nature Research policies, see [Authors & Referees](#) and the [Editorial Policy Checklist](#).

Statistics

For all statistical analyses, confirm that the following items are present in the figure legend, table legend, main text, or Methods section.

n/a Confirmed

- The exact sample size (n) for each experimental group/condition, given as a discrete number and unit of measurement
- A statement on whether measurements were taken from distinct samples or whether the same sample was measured repeatedly
- The statistical test(s) used AND whether they are one- or two-sided
Only common tests should be described solely by name; describe more complex techniques in the Methods section.
- A description of all covariates tested
- A description of any assumptions or corrections, such as tests of normality and adjustment for multiple comparisons
- A full description of the statistical parameters including central tendency (e.g. means) or other basic estimates (e.g. regression coefficient) AND variation (e.g. standard deviation) or associated estimates of uncertainty (e.g. confidence intervals)
- For null hypothesis testing, the test statistic (e.g. F , t , r) with confidence intervals, effect sizes, degrees of freedom and P value noted
Give P values as exact values whenever suitable.
- For Bayesian analysis, information on the choice of priors and Markov chain Monte Carlo settings
- For hierarchical and complex designs, identification of the appropriate level for tests and full reporting of outcomes
- Estimates of effect sizes (e.g. Cohen's d , Pearson's r), indicating how they were calculated

Our web collection on [statistics for biologists](#) contains articles on many of the points above.

Software and code

Policy information about [availability of computer code](#)

Data collection

For blood experiments (life sciences): SQUID magnetometer from Quantum Design MPMS3 (software: MPMS 3 MultiVu v 2.3.3.2); Light transmission aggregometry APACT 4004 (software: Apact LPC V 1.19.10); UV-Vis Spectrometry Agilent Cary 8485 (software: Chemstation B.05.04[8]); AAS Agilent 200 Series AAS (software: SpectrAA v 5.4 Pro); Haematology analyser Sysmex Europe XN-1000 (software: XN-Series version 1993200-52); Phenom Pro Desktop SEM (software: SW version 4.3.3)

Data analysis

Origin Pro 9.0, Excel for Mac v.15.33

For manuscripts utilizing custom algorithms or software that are central to the research but not yet described in published literature, software must be made available to editors/reviewers. We strongly encourage code deposition in a community repository (e.g. GitHub). See the Nature Research [guidelines for submitting code & software](#) for further information.

Data

Policy information about [availability of data](#)

All manuscripts must include a [data availability statement](#). This statement should provide the following information, where applicable:

- Accession codes, unique identifiers, or web links for publicly available datasets
- A list of figures that have associated raw data
- A description of any restrictions on data availability

Source data for figure(s) 2, 3, 4 (and extended data figures containing data graphs) are provided with the paper. Any other data that support the findings of this study are available from the corresponding author upon reasonable request.

Field-specific reporting

Please select the one below that is the best fit for your research. If you are not sure, read the appropriate sections before making your selection.

Life sciences Behavioural & social sciences Ecological, evolutionary & environmental sciences

For a reference copy of the document with all sections, see [nature.com/documents/nr-reporting-summary-flat.pdf](https://www.nature.com/documents/nr-reporting-summary-flat.pdf)

Life sciences study design

All studies must disclose on these points even when the disclosure is negative.

Sample size	For blood pumping studies to determine hemolysis 3 (anonymous) blood donors each donated 50 mL, which was used to make 6 mL samples for each series of experiments (see section M17 for a more detailed description). For studies to determine whether magnetite nanoparticles were transferred from the ferrofluid to the blood during pumping 2 anonymous donors were used.
Data exclusions	Three Qpumps were made (using 3D printing / glued magnet arcs, see section M16). Pump number 3 made loud mechanical noises and its rotation was irregular. All data obtained using pump number 3 was discarded for that reason.
Replication	Blood pumping experiments were done on the same Qpumps, using different blood donors, and on different days/weeks. The results were always consistent.
Randomization	No randomization was used.
Blinding	No blinding was used.

Reporting for specific materials, systems and methods

We require information from authors about some types of materials, experimental systems and methods used in many studies. Here, indicate whether each material, system or method listed is relevant to your study. If you are not sure if a list item applies to your research, read the appropriate section before selecting a response.

Materials & experimental systems

n/a	Involvement in the study
<input checked="" type="checkbox"/>	<input type="checkbox"/> Antibodies
<input checked="" type="checkbox"/>	<input type="checkbox"/> Eukaryotic cell lines
<input checked="" type="checkbox"/>	<input type="checkbox"/> Palaeontology
<input checked="" type="checkbox"/>	<input type="checkbox"/> Animals and other organisms
<input type="checkbox"/>	<input checked="" type="checkbox"/> Human research participants
<input checked="" type="checkbox"/>	<input type="checkbox"/> Clinical data

Methods

n/a	Involvement in the study
<input checked="" type="checkbox"/>	<input type="checkbox"/> ChIP-seq
<input checked="" type="checkbox"/>	<input type="checkbox"/> Flow cytometry
<input checked="" type="checkbox"/>	<input type="checkbox"/> MRI-based neuroimaging

Human research participants

Policy information about [studies involving human research participants](#)

Population characteristics	Blood donors were anonymous, and consist of male / female healthy adults that regularly donate blood to the French blood center (EFS). See ethics oversight below.
Recruitment	A dozen of donors come to the French blood center (EFS) in Strasbourg every day. No specific recruitment or selection was done for this study.
Ethics oversight	Human studies were performed according to the Helsinki Declaration. Control human samples were obtained from volunteer blood donors who gave written informed consent recruited by the blood transfusion center where the research was performed (Etablissement Français du Sang-Grand Est). Patients were recruited at the University Hospital of Strasbourg and signed a statement giving informed consent (no. CODECOH: DC-2015-2368, Comité de Protection des personnes Est-IV no. 15/50 du 15/02/2016) that residual blood collected for classical care can be used for research purposes after irreversible anonymization.

Note that full information on the approval of the study protocol must also be provided in the manuscript.